2025-06-23

Low Surface Brightness Features of Edge-on Galaxies in Deep Sky Surveys

Kyle R. Adams
Brigham Young University

Low Surface Brightness Features of Edge-on Galaxies in Deep Sky Surveys

Kyle R Adams

A thesis submitted to the faculty of
Brigham Young University
in partial fulfillment of the requirements for the degree of

Master of Science

Aleksandr Mosenkov, Chair
Denise Stephens
Darin Ragozzine
Benjamin Boizelle

Department of Physics and Astronomy

Brigham Young University

ABSTRACT

Low Surface Brightness Features of Edge-on Galaxies in Deep Sky Surveys

Kyle R Adams
Department of Physics and Astronomy, BYU
Master of Science

In this thesis, we present a comprehensive visual analysis of low surface brightness (LSB) structures in edge-on galaxies using two statistically complete samples: 838 galaxies from the SDSS Stripe 82 region (ES82) and 5,745 galaxies from the Edge-on Galaxies in SDSS (EGIS) catalog, both containing galaxies with spectroscopic redshifts out to $z \sim 0.2$. Using deep imaging data from the SDSS, SDSS Stripe 82, DESI Legacy Imaging Surveys, and the HSC-SSP, we construct RGB and coadded images for comparison and to improve feature detection. Average limiting photometric depth for each survey in the r band for the surveys analyzed in this study are, 26.5 mag arcsec^{-2}, 28.6 mag arcsec^{-2} for SDSS Stripe 82, 28.5 mag arcsec^{-2} for DESI, and 29.7 mag arcsec^{-2} for HSC-SSP. For the EGIS sample, additional deep images from the APO 3.5m telescope were incorporated for a subsample of galaxies with dim tidal features, reaching a depth of 29.4 mag arcsec^{-2} in the r band. All images and classifications are compiled into the largest atlas of features around edge-on galaxies to date. A custom semi-automatic pipeline and graphical user interfaces (GUIs) were developed for image analysis and classification refinement. We find that 5.8% of the Stripe 82 galaxies show LSB tidal structures, while only 2.8% of the EGIS sample exhibits such features. These fractions are significantly lower than predictions from most cosmological simulations, which estimate 20–40% incidence at similar surface brightness limits. Our results suggest that the low detection rates may reflect a genuine scarcity of tidal structures rather than limitations in observational depth or sample composition. Furthermore, a large portion of both samples consists of late-type galaxies, which may contribute to the discrepancy, as early-type galaxies more commonly host visible tidal features. This work highlights the need to reassess simulation assumptions and motivates future studies using deeper surveys, such as LSST, to bridge the gap between observation and theory further. Additionally, we classify disk warps as having an angle amplitude $\geq 3°$ and disk lopsidedness as having a radii ratio ≥ 0.10 at isophotes of 24 and 26 mag arcsec^{-2}, finding occurrence fractions of 42.8% and 34.2% using the 26 mag arcsec^{-2} isophote, respectively, consistent with prior observational studies. However, unlike previous work, which often finds S-type warps to be more common, we observe a much lower fraction of S-type warps, only 7.1% in the EGIS sample, compared to the ~ 30% reported by other studies.

Keywords: [Galaxies: evolution - formation - halos - interactions - photometry - structure]

ACKNOWLEDGMENTS

I would like to thank Dr. Aleksandr Mosenkov for taking me on as his graduate student and helping and guiding me so I could complete my master's. I would also like to thank Maria Skryabina for all her help and work on the paper that we published (Stripe 82), on which this thesis is based. I would also like to thank Thea Spigarelli, Lydia Stacey, and Brandon Burton for their work in helping to classify and measure characteristics of galaxies. Additionally, I would like to thank Elisabeth Sola for providing the statistics for their tidal structures from their study Sola et al. (2022), which will be included in a future paper. Furthermore, I would like to thank the members of my graduate advisory committee for their support and for reviewing this work and providing feedback.

This research has made use of the NASA/IPAC Extragalactic Database (NED; https://ned.ipac.caltech.edu/), the HyperLEDA database (http://leda.univ-lyon1.fr/; Makarov et al. 2014), various data releases from the Sloan Digital Sky Survey (SDSS) (https://www.sdss.org/), various data releases from the Legacy Surveys which consist of three individual and complementary projects: the Dark Energy Camera Legacy Survey (DECaLS), the Beijing-Arisona Sky Survey (BASS), and the Mayall z-band Legacy Survey (MzLS). This research used data obtained with the Dark Energy Camera (DECam). This research is based on data collected at the Subaru Telescope and retrieved from the HSC data archive system.. This research makes use of software developed for the Vera C. Rubin Observatory. We thank the Rubin Observatory for making their code available as free software at http://pipelines.lsst.io/. This research makes use of observations obtained with the Apache Point Observatory 3.5-meter telescope, which is owned and operated by the Astrophysical Research Consortium. This research has made use of the VizieR catalogue access tool, CDS, Strasbourg Astronomical Observatory, France (https://doi.org/10.1051/aas:2000169) This research makes use of data products from the Two Micron All Sky Survey (Skrutskie et al. 2006), which is a joint project of the University of Massachusetts and the Infrared Processing and Analysis Center/California Institute of Technology, funded by the National Aeronautics and Space Administration and the National Science Foundation.

Contents

List of Figures

List of Tables

Chapter 1

Introduction

In the hierarchical model of structure formation, galaxies grow and evolve primarily through interactions with other galaxies. This includes major and minor mergers, flybys, and accretion of surrounding material, ultimately forming larger systems (Kado-Fong et al. 2018; Kumar et al. 2021; L'Huillier et al. 2012; Martin et al. 2018). To clarify these mechanisms, major mergers occur when two or more galaxies of comparable mass collide and coalesce, often resulting in dramatic structural transformations. Minor mergers involve the interaction of a large galaxy with a significantly smaller companion or several dwarf galaxies. Flybys describe close encounters between galaxies that do not result in a merger but can still lead to substantial morphological disturbances due to their high-speed gravitational interaction (Kumar et al. 2021). Lastly, accretion refers to the gradual accumulation of matter, either through the inflow of cold gas from the cosmic web (Dekel et al. 2009; Martin et al. 2016) or via material transferred from a neighboring, often smaller, donor galaxy (Oser et al. 2010).

This evolutionary framework is supported by cosmological simulations based on the standard ΛCDM model, which successfully explains the formation and growth of large-scale structures in the universe. According to this model, the universe evolved from a hot, dense, and nearly homogeneous state following the Big Bang into the present-day cosmic web, characterized by an intricate network of filaments, walls, and voids (Frenk & White 2012). Cosmological hydrodynamical simulations

have shown that galaxy interactions leave behind characteristic low surface brightness (LSB) tidal features (see e.g. Toomre & Toomre 1972, Quinn 1984, Mancillas et al. 2019a). This has also been verified through many observational studies (e.g. Schwarzkopf & Dettmar 2000, Martínez-Delgado et al. 2010, Jackson et al. 2023) and simulations (e.g. Schaye et al. 2015, Pillepich et al. 2019, Mancillas et al. 2019a). As tracers of galaxy interactions, LSB features can be used to reconstruct how a host galaxy has evolved. This is important for understanding the main mechanisms that drive galaxy evolution today and in the past. It also serves as a way to verify and compare current models of the evolution of the universe (Martin et al. 2022).

In the past, LSB features around galaxies were difficult to identify because they are usually too dim (fainter than $\sim 25-26$ mag arcsec^{-2} in the r band (Brough et al. 2020) to be seen on regular photometric exposures. To add to the difficulty, some filaments of Galactic cirrus can be mistakenly identified as extragalactic LSB features (Sollima et al. 2010). Cirrus clouds are typically found at Galactic latitudes greater than 20 degrees and represent dusty filaments that do not have a particular shape. These clouds derive their name from their similarity in appearance to the cirrus clouds of Earth. Milky Way cirrus clouds can be well-seen in deep optical images and, thus, can hinder the detection and study of LSB galaxy structures. On the other hand, deep imaging is of high importance for studying the properties of Galactic cirrus (see e.g. Miville-Deschênes et al. 2016, Román et al. 2020, Marchuk et al. 2021, Smirnov et al. 2023).

Due to the difficulties discussed above and many others (e.g., sky background contamination, instrumental scattered light, observational issues related to long exposures), deep optical observations of galaxies are problematic. However, improvements in CCD and telescope technology have now made it possible to discern structures whose surface brightness reaches 29–30 mag arcsec^{-2} (see e.g. Martínez-Delgado et al. 2010, Abraham & van Dokkum 2014, Duc et al. 2014, Rich et al. 2019). New techniques in processing deep images, including a non-aggressive sky-subtraction method (Fliri & Trujillo 2016) and taking into account the point spread function (PSF; Jiang et al. 2014,

Annis et al. 2014, Trujillo & Fliri 2016), have become useful methods for combining images that give better depth and resolution. Because of the development of this field of deep photometry over the past 15–20 years, studies based on deep and ultra-deep images of space objects have begun to play a relevant role in the study of the Universe (see e.g., Mihos et al. 2005, Illingworth et al. 2013, Abraham & van Dokkum 2014, van Dokkum et al. 2015, Koda et al. 2015, Poliakov et al. 2021).

Modern sky surveys such as the Sloan Digital Sky Survey (SDSS, York et al. 2000) and the much deeper DESI Legacy Imaging Surveys (Dey et al. 2019) have provided a plethora of data for extragalactic studies. These expansive datasets have opened new avenues for identifying and analyzing previously undetectable extragalactic structures. One study by Karachentsev & Kaisina (2022), using DESI Legacy, found 67 new LSB dwarf galaxy candidates that had previously gone undetected. Another study by Martínez-Delgado et al. (2023), using DESI Legacy, investigated 3,100 galaxies and discovered 24 new LSB features. While large surveys are invaluable for broad statistical studies, targeted deep observations of individual galaxies can also reveal the importance of imaging depth in characterizing faint structures. A compelling example is the case of the well-known edge-on galaxy NGC 5907, famous for the faint tidal stream that wraps around it. Martínez-Delgado et al. (2008) observed the galaxy at a depth of approximately 28.7 mag arcsec^{-2} while van Dokkum et al. (2019) observed the galaxy at a depth of 30.3 mag arcsec^{-2} with the comparison of both observations in Fig. 1.1. The latest study done by van Dokkum et al. (2019) revealed that the second loop of the stream seen in Martínez-Delgado et al. (2008) was missing. van Dokkum et al. (2019) also reveals a stream that extends beyond the host galaxy. Such studies highlight the importance of using deep sky surveys for studying faint structures and objects. The upcoming Legacy Survey of Space and Time (LSST, Ivezić et al. 2019) will further enhance our ability to image galaxies, promising even deeper and more comprehensive observations at depths of 30 mag arcsec^{-2} and greater that could unveil extremely faint extragalactic structures.

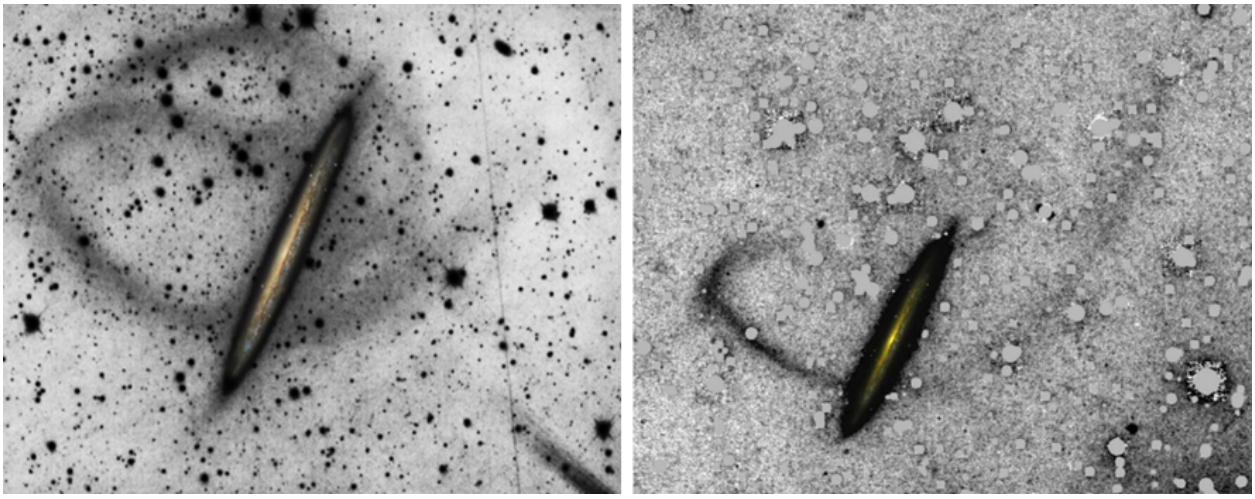

Figure 1.1 Deep images of the galaxy NGC 5907. The image on the left, provided by Martínez-Delgado et al. (2008), has a depth of approximately 28.7 mag arcsec^{-2}. The image on the right, provided by van Dokkum et al. (2019), has a depth of 30.3 mag arcsec^{-2}.

Deep optical observations of edge-on galaxies using such surveys provide an unprecedented view of the luminous matter distribution in galaxies (van der Kruit & Searle 1981, de Grijs 1998, Dalcanton & Bernstein 2002, Kregel et al. 2002, Mosenkov et al. 2010, Bizyaev et al. 2014). This view allows LSB features to be seen with increased visual clarity, especially above and below the galaxy mid-plane, unlike face-on galaxies where faint structures are much less apparent over the galaxy body and only become discernible far beyond the optical radius (Fry et al. 1999, van Dokkum et al. 2019, Mosenkov et al. 2020a, Gilhuly et al. 2020, Mosenkov et al. 2020b, Martínez-Delgado et al. 2021, Gilhuly et al. 2022, Mosenkov et al. 2022). Specific structures, such as disk warps, can only be reliably identified when galaxies are viewed edge-on (Reshetnikov et al. 2016a). Moreover, this view limits the projection effects introduced through random inclination angles in a sample of galaxies (Mosenkov et al. 2020a).

1.1 Overview of Project

Cosmological simulations using the ΛCDM model have had great success at reproducing general galaxy properties and scaling relationships as well as tidal features (Somerville & Davé 2015). However, simulations still show differences from observation, such as the longstanding discrepancy of the star formation rate vs. stellar mass relation that gives a steeper slope than observed for lower mass galaxies at intermediate redshifts (Daddi et al. 2007, Christensen et al. 2012, Somerville & Davé 2015). This could mean that our understanding of the processes regulating star formation needs to be revised (Somerville & Davé 2015). This is why it is important to use observations to fine-tune simulations. Observations of LSB tidal features can be used to check predictions from simulations. Johnston et al. (2001) used ΛCDM cosmological galaxy formation simulations to predict that approximately 20–40% of $z \sim 0$ galaxies are expected to have tidal features. Martin et al. (2022) constrains this to 25% for a similar limiting surface brightness of 28 mag arcsec^{-2}. Additionally, Valenzuela & Remus (2022) found a tidal feature fraction of 23%.

Despite reaching comparable surface brightness limits, numerous observational LSB studies of tidal features report much lower detection rates. For instance, Kado-Fong et al. (2018) identified tidal features in only 5.6% of their sample, a value significantly below the conservative simulation-based estimate of 23%. This discrepancy does not necessarily indicate a flaw in the ΛCDM framework; rather, it may reflect limitations in current observational capabilities, such as insufficient imaging depth, small sample sizes, or bias in the sample against systems with LSB features. To better assess this gap between theory and observation, more extensive datasets from deeper surveys are essential.

The primary goals of this thesis are to investigate the occurrence and properties of LSB tidal and structural features in edge-on galaxies using two large datasets taken from deep sky surveys and to create the largest atlas of features around edge-on galaxies ever created. We use deep, high-quality imaging data from multiple modern sky surveys, the Sloan Digital Sky Survey (SDSS), the Hyper Suprime-Cam Subaru Strategic Program (HSC-SSP), and the Dark Energy Spectroscopic Instrument

(DESI) Legacy Imaging Surveys, to refine our classifications of features. We also seek to compare the occurrence fraction of features within our samples to cosmological simulations to investigate the mismatch between predictions from cosmological simulations, which estimate a 20–23% tidal feature occurrence rate, and observational studies that report lower detection rates. This thesis seeks to confirm this discrepancy and to assess whether it arises from limitations in observational data, classification methods, or possible issues within simulations themselves. Understanding this discrepancy is important, as it could lead to better cosmological simulations and, therefore, to a better understanding of galaxy evolution. Furthermore, this work introduces two Graphic User Interfaces (GUIs) that were developed to improve methodologies for measuring structural features, ultimately contributing to a more robust comparison between theoretical predictions and empirical evidence.

The structure of this thesis is as follows. Chapter 2 defines each LSB feature and structural characteristic that is used in this thesis. Chapter 3 outlines the image preparation and processing methods applied to the Stripe 82 dataset. It also presents the resulting catalog, provides statistical insights into the structural classifications, and summarizes key findings. Chapter 4 details the image processing steps for the EGIS sample across multiple deep surveys, introduces updated approaches to classifying warps and lopsided galaxies, and presents the largest atlas of features around edge-on galaxies to date. Chapter 5 gives an in-depth analysis of the results. Finally, Chapter 6 concludes with a comprehensive summary of findings from both galaxy samples.

Chapter 2

The Nomenclature of Low Surface Brightness Features

In this thesis, we investigate two categories of features: those created from tidal interactions known as tidal structures and those formed from other processes — distinct internal structural features. It should be noted that both categories may be related to galaxy interactions and thus we consider them together. The type of structure, information about it, and an example will be given below.

2.1 Tidal Structures

Tidal Tails and Streams

In deep optical images, tidal tails and streams appear as extended filaments emanating from the host galaxy. These two structures appear similar to each other, but have distinct characteristics and formation histories. Tidal tails manifest as broad, fan-like extensions of stars and gas that emanate from galactic disks, often appearing in symmetric pairs trailing from an interacting system (Toomre & Toomre 1972, Barnes 1992, Mancillas et al. 2019b). Tidal tails result from the merging and

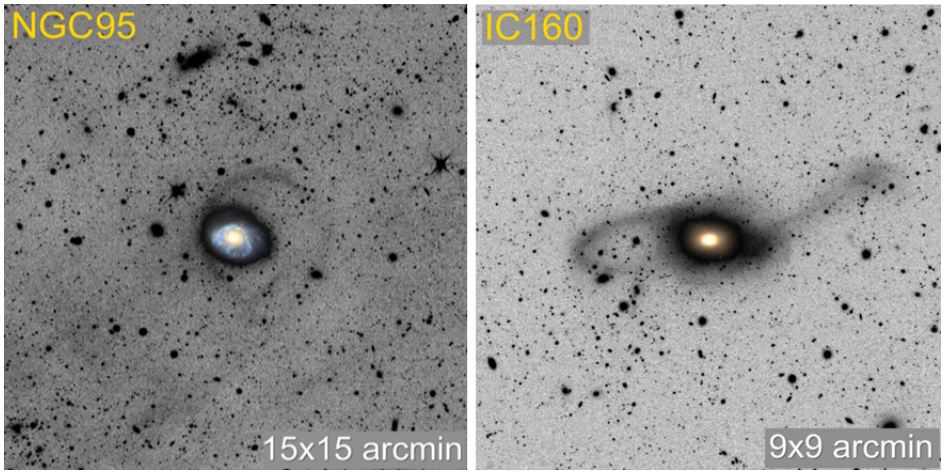

Figure 2.1 The left galaxy image exhibits a stellar stream, while the galaxy image on the right exhibits a tidal tail on the right side of the host galaxy. Both images are taken from Martínez-Delgado et al. (2023).

interaction of galaxies, typically through major mergers (Bílek et al. 2020; Byrd & Howard 1992; Duc & Renaud 2013; Oh et al. 2015). In optical imaging, tails are often blue and clumpy, reflecting in situ star formation in dense condensations along the tail, although older stellar populations from the disk also contribute (Rodruck et al. 2023).

In contrast to tails, stellar streams are narrow, coherent filaments of debris that can wrap partially or fully around a host galaxy, arising from tidal disruption of low-mass satellites interacting with the host galaxy (Johnston et al. 1996, Majewski et al. 1999, McConnachie et al. 2009, Duc et al. 2014). Streams also exhibit low metallicity, as they are mainly comprised of older stars and lack star-forming regions (Duc et al. 2014). Mancillas et al. (2019b) find that tails are more short-lived than streams. Examples of tails and streams can be seen in Fig. 2.1.

Diffuse Shells, Plumes, or Asymmetric Stellar Halos

Diffuse shells appear as faint, concentric, sharp-edged arcs or ripples that predominantly appear in early-type galaxies (ETG) (Ebrova 2013, Pop et al. 2018,Yoon et al. 2024). The main formation mechanism of shells is not fully understood, but they are believed to be formed by major or minor

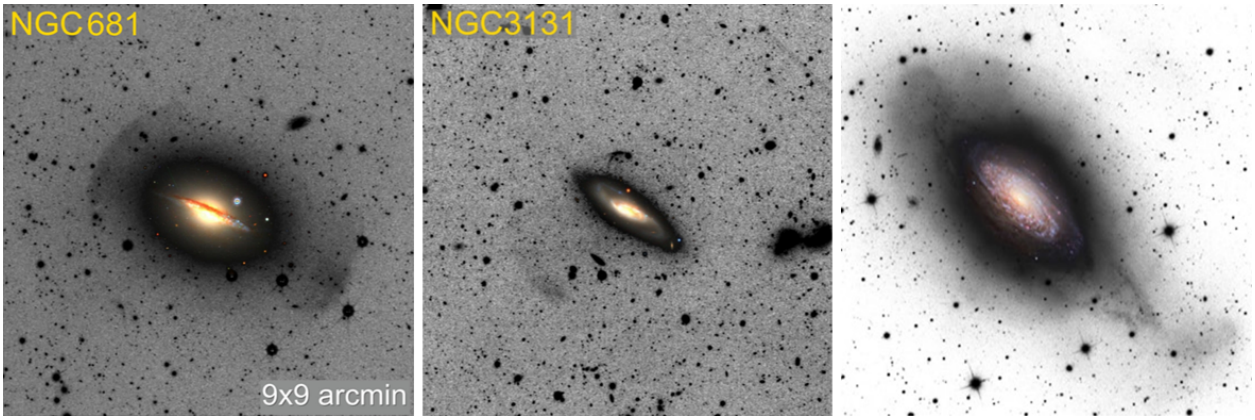

Figure 2.2 The left and middle images exhibit a shell and plume, respectively, and are taken from Martínez-Delgado et al. (2023). The right image is an example of an asymmetric stellar halo taken Martínez-Delgado et al. (2010).

mergers (Ebrova 2013, Pop et al. 2018). In cases where diffuse shells form through minor mergers, they typically arise from the accretion of low-mass satellite galaxies on nearly radial orbits (Prieur 1990, Cooper et al. 2011, Ebrova 2013, Pop et al. 2018). Examples of diffuse shells can be seen in Fig. 2.2.

Plumes are broad, diffuse fans of starlight that extend to one side of the main body of the galaxy, lacking the clear concentric geometry of shells, but both types of features are possibly related. Asymmetric stellar halos are characterized by the absence of clearly defined structures such as stellar streams, tails, or shells, and often exhibit an overall asymmetry in the stellar halo (Martin et al. 2022, Khalid et al. 2024).

Bridges

Bridges appear as elongated structures of stars and gas reaching from one galaxy to another, possibly connecting the two galaxies and exchanging material. Bridges can be more pronounced in HI and typically contain star-forming regions (Smith et al. 1997, Marziani et al. 2003). Bridges can form from flybys or the processes of a merger. These interactions can also form tails if the galaxies are

Figure 2.3 The image on the left exhibits a bridge connecting NGC 5574 and NGC 5576, causing the stream. The image on the right exhibits a bridge connecting NGC 5507 on top to NGC 5506 on the bottom. Both images are taken from Duc et al. (2015).

similar in size (Toomre & Toomre 1972, Smith et al. 2010, Barrabés et al. 2017). Examples of bridges can be seen in Fig. 2.3.

Single Arcs and Loops

Arcs and loops are types of stellar streams that are wrapped around the host galaxy. They can be produced by dynamical friction (Boylan-Kolchin et al. 2008) and tidal stripping (Peñarrubia et al. 2008) and can be signs of a past or ongoing minor merger (Martínez-Delgado et al. 2010). Examples of arcs and loops can be seen in Fig. 2.4.

Tidally Distorted Satellites or Satellite Debris

Tidally distorted satellites or satellite debris are the remnants of satellite galaxies that were disrupted by the process of tidal interaction with their host galaxy (see Mateo et al. 1998, Majewski et al. 1999, Johnston et al. 2001, Rich et al. 2012, Sanders et al. 2018). Examples of satellite debris can be seen in Fig. 2.5.

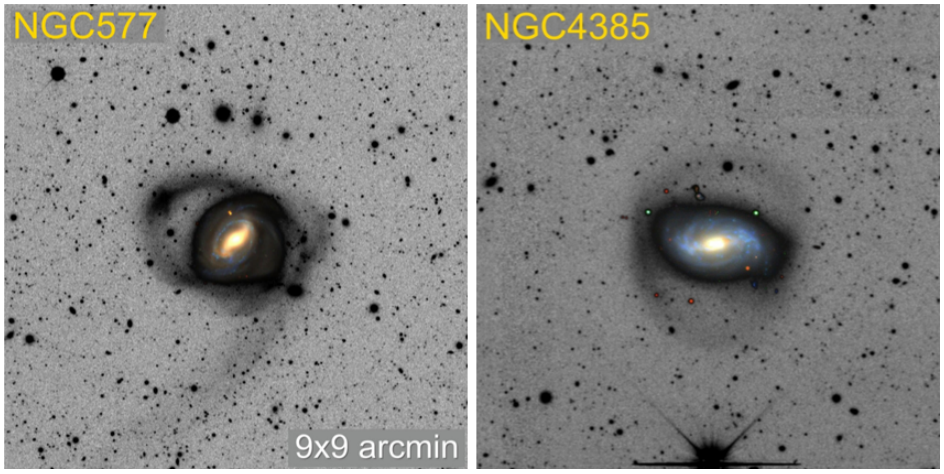

Figure 2.4 The galaxy image on the left exhibits a single arc stellar stream, while the galaxy in the image on the right exhibits a faint loop. Both images are taken from Martínez-Delgado et al. (2023)

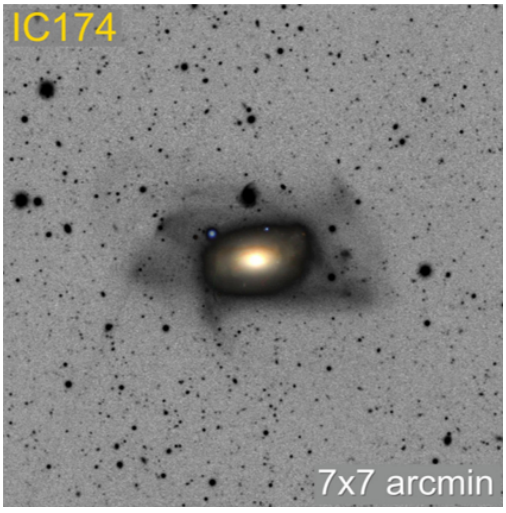

Figure 2.5 An example of a satellite galaxy that is being tidally disrupted and absorbed by its host. Image taken by Martínez-Delgado et al. (2023).

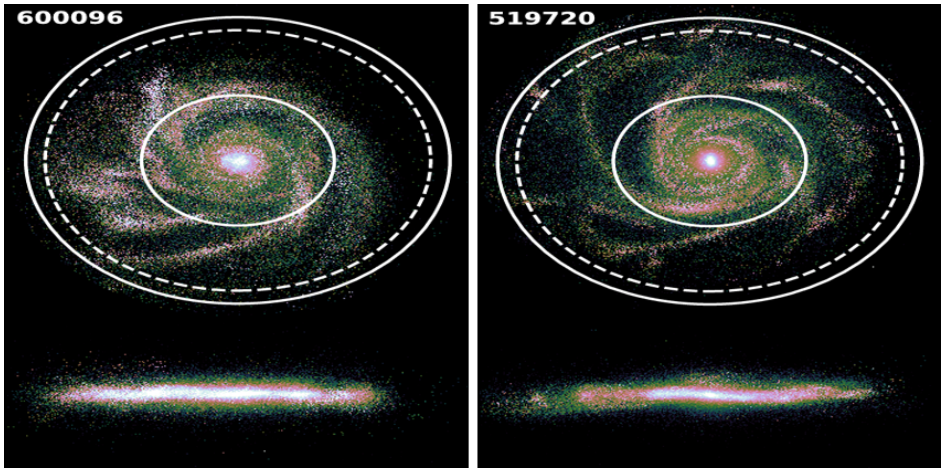

Figure 2.6 Both images exhibit a simulated lopsided disk with the face-on view on top and the edge-on view at the bottom. The solid white circle represents the 29 mag arcsec^{-2} isophotal radius while the dashed line depicts the 26.5 mag arcsec^{-2} radius. Both images are taken from Varela-Lavin et al. (2023).

2.2 Distinctive Structural Features

Lopsided Disks

Lopsided galaxy disks exhibit significant disk asymmetries along the galaxy plane relative to the galaxy center (Baldwin et al. 1980, Bournaud et al. 2005, Sancisi et al. 2008). The most likely scenario of their formation involves asymmetric gas accretion (Jog & Combes 2009, Łokas 2022). In most studies, the lopsidedness is measured as the amplitude A_1 of the Fourier mode $m = 1$ applied to the surface density (Bournaud et al. 2005, Łokas 2022, Dolfi et al. 2023). In this thesis, we use a more straightforward approach by measuring the pixel radii of the galaxy's disk using the 26 mag arcsec^{-2} isophote and calculating the ratio of the absolute value of the difference between the left and right radii and the smallest radius. Examples of lopsided disks are shown in Fig. 2.6.

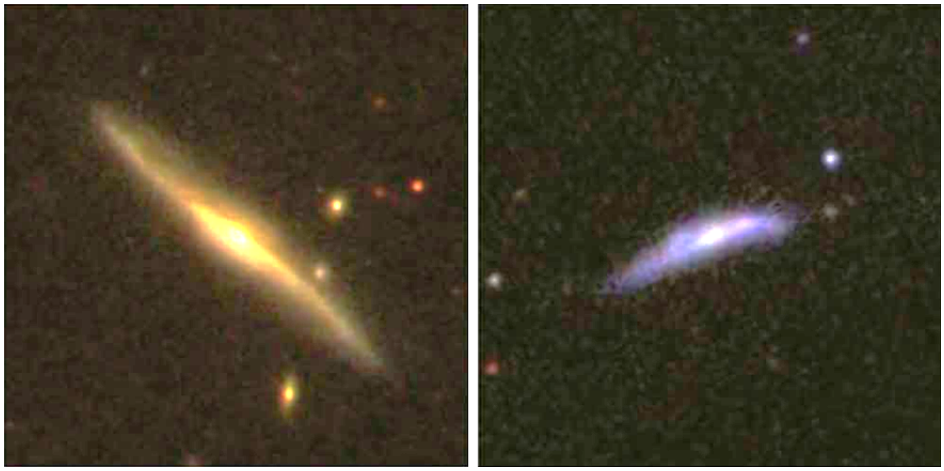

Figure 2.7 The galaxy image on the left exhibits an S-type warp, while the galaxy in the image on the right exhibits an L-type warp. Both images are taken from Zee et al. (2022).

Disk Warps

Disk warps are a departure of the disk matter from the mean galactic plane, which becomes especially prominent at the galaxy periphery (Sánchez-Saavedra et al. 1990, Reshetnikov & Combes 1998, Reshetnikov et al. 2002, Gómez et al. 2017). The warps can appear as S-shaped, U-shaped, or L-shaped disks, with the U-shaped and L-shaped warps often being defined as one category (Reshetnikov & Combes 1998, Ann & Park 2006, Zee et al. 2022, Reshetnikov et al. 2025). Disk warps are quite common and appear in 40–50% of all galactic disks (Mosenkov et al. 2020b, Zee et al. 2022). Even though disk warps are typically much more pronounced in HI beyond the optical disk, optical warps can still provide reasonable detection and measurement (van der Kruit 1979, Reshetnikov et al. 2016b). A disk warp may arise from a misalignment between the disk and its surrounding dark matter halo, which can vary over time due to precession (Weinberg & Blitz 2006). Alternatively, the warp could result from interactions with satellites (Zee et al. 2022), accretion, or fast tidal interactions (Mosenkov et al. 2020b). Examples of disk warps can be seen in Fig. 2.7.

In this work, warps are also categorized into two types based on their "thickness": thin and thick warps. Thick warps are grouped under the broader tidal feature classification labeled "Disk

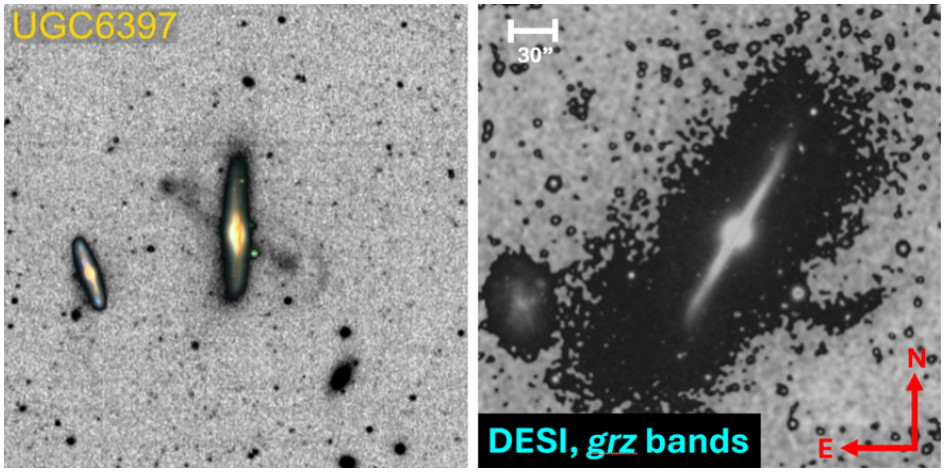

Figure 2.8 The galaxy image on the left exhibits a polar ring and is taken from Martínez-Delgado et al. (2023). The galaxy image on the right exhibits a polar bulge and is taken from Bahr & Mosenkov (2025).

Deformations”, as they may be indicators of tidal interactions (Semczuk et al. 2020). In particular, the intrinsic thickness of the disk can increase as a result of minor mergers (Qu et al. 2011, Villalobos & Helmi 2008, Semczuk et al. 2020).

Polar Structures

Polar structures include different types of structures, such as polar rings/disks, polar bulges, and polar halos (Mosenkov et al. 2024), but in this study, we only focus on the two most common features, polar rings and polar bulges. Polar rings represent large-scale inner or outer rings or disks of gas, dust, and stars, orbiting in the plane approximately perpendicular to the disk of the host galaxy (Whitmore et al. 1990, Reshetnikov & Sotnikova 1997, Moiseev et al. 2011, Reshetnikov & Combes 2015). Galaxies described as having polar bulges display a major axis that is markedly tilted relative to the disk’s major axis. Their morphology bears a close resemblance to polar-ring galaxies, but polar bulges appear to be less luminous analogs of the hosts in polar-ring galaxies (Reshetnikov et al. 2015). Several formation scenarios have been proposed to explain polar structures. These include the accretion of material from a companion galaxy, either through tidal stripping (Schweizer

et al. 1983, Reshetnikov & Sotnikova 1997) or disruption of a gas-rich satellite on a perpendicular orbit (Rix & Katz 1991, Katz & Rix 1992); the merger of two galaxies of comparable mass (Bekki 1997, Bekki 1998, Bournaud & Combes 2003); and the misaligned accretion of gas from cosmic filaments onto the host galaxy (Macciò et al. 2006, Brook et al. 2008). Examples of polar structures can be seen in Fig. 2.8.

Chapter 3

Tidal Features of Edge-on Galaxies in the SDSS Stripe 82

This chapter contains information from the paper "Tidal features and disk thicknesses of edge-on galaxies in the SDSS Stripe 82" (Skryabina et al. 2024), which was authored by Maria N. Skryabina and co-authored by me and Dr. Mosenkov. From here on, it will be referenced in later chapters as the Stripe 82 paper, and the data therein as the Stripe 82 sample. This paper, to which I made a significant contribution, forms the foundation of my master's thesis. The following sections and images are taken directly from the paper itself, excluding the original introduction and sections discussing disk thickness. Sections, to which I did not contribute, have been rewritten and included solely for context.

In the following study, we created a new catalog of edge-on galaxies selected from the deep SDSS Stripe 82, ES82 for short. This work identified LSB features around the selected galaxies taking into account cirrus contamination (Smirnov et al. 2023) and excluding sources identified in complementary deep imaging. We compared the percentage of tidal features from our catalog to

those in recent papers that considered galaxies at a wide range of orientations as well as results from modern cosmological hydrodynamical simulations.

3.1 The Sample and Data

The SDSS Stripe 82 (Jiang et al. 2014), located along the celestial equator, spans 2.5 degrees in width and covers Right Ascension from –50° to 60° and declination from –1.25° to 1.25°, amounting to a total area of 275 square degrees across all five SDSS photometric bands. What makes Stripe 82 especially useful for our analysis is its increased imaging depth. While standard SDSS observations typically reach a surface brightness limit of around 26.5 mag arcsec^{-2} in the r band, Stripe 82 achieves a significantly deeper limit of 28.6 mag arcsec^{-2}, based on data from the IAC Stripe 82 Legacy Project[1]. As demonstrated in this study and supported by previous work (Fliri & Trujillo 2016; Martínez-Lombilla & Knapen 2019; Yesuf et al. 2021; Zaritsky et al. 2021), this depth enables detailed investigation of faint, extended structures surrounding galaxies.

Several initiatives have focused on processing or reprocessing images from the SDSS Stripe 82 region. Among these, the IAC Stripe 82 Legacy Project (Fliri & Trujillo 2016) stands out for its use of a careful, minimally invasive sky background subtraction method, designed to retain faint, extended features across a broad range of spatial scales and intensities. Utilizing the high-quality imaging from this project, we have constructed a detailed catalog of edge-on galaxies located in the deep Stripe 82 field, ES82. This dataset offers a valuable foundation for investigating subtle, low-surface brightness structures, such as stellar streams, tidal tails, arcs, shells, bridges, and disk distortions. These structures often reveal signatures of past or ongoing interactions between galaxies and their environments.

[1] http://research.iac.es/proyecto/stripe82/

3.1.1 Selection of Galaxies

To assemble the ES82 sample, we utilized multiple sources to identify suitable edge-on galaxies within this region. A primary resource was the set of SExtractor (Bertin & Arnouts 1996) catalogs in the r band (Fliri & Trujillo 2016), which includes Stripe 82. Our goal was to isolate galaxies with both a large angular size and a low apparent axis ratio. Since SExtractor does not provide direct measurements of a galaxy's optical diameter, we relied on the Kron radius (r_{Kron}) as a proxy for angular size during selection. The Kron radius, introduced by Kron (1980), is a flux-weighted radius that approximates the size of an object by integrating its light profile, typically encompassing the majority of the total flux. Drawing on findings from the EGIS and EGIPS catalogs (Bizyaev et al. 2014; Makarov et al. 2022), we adopted a set of selection criteria requiring a Kron radius greater than 15 arcsec and an axis ratio (semi-minor axis/semi-major axis) less than 0.3 (corresponds to inclinations ranging from 80° to 90°). These parameters are intended to identify large edge-on ($i \geq 85°$) or nearly edge-on ($80° \leq i < 85°$) galaxies, allowing us to resolve and analyze their vertical structures in greater detail.

To further refine our sample, we cross-referenced our automated selection with additional established datasets. Specifically, we consulted the EGIS catalog (Bizyaev et al. 2014) and the Galaxy Zoo project (Hart et al. 2016), considering only galaxies for which >80% of Galaxy Zoo participants classified the object as "edge-on." This step was taken to confirm that our selection criteria consistently identified edge-on systems. We also manually reviewed the catalog of approximately 17,000 galaxies compiled by Bottrell et al. (2019) for the Stripe 82 region. This visual screening allowed us to identify additional edge-on candidates and remove duplicate entries from our preliminary list by comparing object coordinates across all sources.

Following the sample refinement, we generated RGB composite images for each selected galaxy using data from three surveys: SDSS Stripe 82 (Fliri & Trujillo 2016), the Hyper Suprime-Cam Subaru Strategic Program (HSC-SSP) PDR3 (Aihara et al. 2022), and the DESI Legacy Imaging

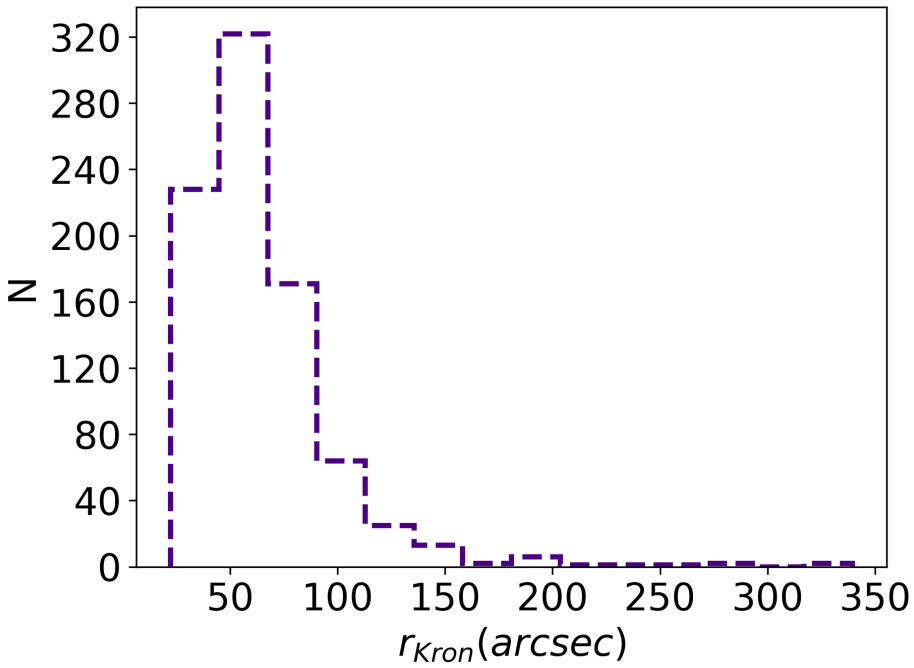

Figure 3.1 Kron radius distribution for galaxies from the ES82 catalog.

Surveys (Dey et al. 2019). Details of the image generation methodology are provided in Sect. 3.1.2. It is important to note that the Stripe 82 footprint is not uniformly covered by the HSC-SSP and DESI Legacy surveys, a limitation discussed further in Sect. 3.1.2. We conducted a visual inspection of the RGB images to ensure the reliability of our final sample, removing any objects that mimicked edge-on morphology due to imaging artifacts, bright star diffraction spikes, or misleading spiral features. Galaxies with moderate inclinations (i.e., with $i \lesssim 80^{\circ}$) identified by characteristics such as visible spiral arms, pure (non-disky) outermost isophotes, or offset dust lanes were also excluded. After this rigorous visual vetting process, we finalized a catalog of 838 confirmed edge-on or nearly edge-on galaxies, drawn from an initial sample of 1,167 candidates. The distribution of galaxy sizes within the final catalog is illustrated in Fig. 3.1.

3.1.2 Data and Preparation

We made use of sky-rectified images across the g, r, i, and r-deep bands, along with their corresponding empirical point spread function (PSF) images and associated weight maps with a pixel scale of 0.396 arcsec. These datasets are essential for conducting detailed photometric decompositions of the galaxies. In the coadded dataset, the r band images reach a mean surface brightness threshold of 28.6 mag arcsec^{-2} where the depth is evaluated at the 3σ level using a 10×10 arcsec^2 region, which has become a common metric for assessing photometric depth for results obtained across different instruments (Román et al. 2020). The average full width at half maximum (FWHM) for the r band images is 1.10 arcsec.

To improve the morphological classification of galaxies in our sample, we incorporated data from two additional deep sky surveys: the DESI Legacy Imaging Surveys (Dey et al. 2019) and the Hyper Suprime-Cam Subaru Strategic Program (HSC-SSP) (Aihara et al. 2022).

The HSC-SSP, which utilizes the Hyper Suprime-Cam mounted on the 8.2-meter Subaru Telescope, operates in three observational modes — Wide (1400 deg^2, reaching $r \sim 26$ mag at 5σ), Deep (27 deg^2, $r \sim 27$ mag), and UltraDeep (3.5 deg^2, $r \sim 28$ mag). The HSC system features 104 CCDs and covers a 1.5-degree field of view with a pixel scale of 0.168 arcsec. The improved spatial resolution and depth of the coadded data enhance our ability to detect faint, extended features, achieving a mean r band surface brightness sensitivity of 29.6 ± 0.4 mag arcsec^{-2}.

The DESI Legacy Imaging Surveys DR9, comprising the DECaLS, BASS, and MzLS components, span approximately 14,000 deg^2 of the extragalactic sky, covering both northern and southern hemispheres in the g, r, and z bands. For the subset of galaxies in our study, the r band data exhibit an average surface brightness depth of 28.4 ± 0.3 mag arcsec^{-2}.

Due to the partial overlap among the IAC Stripe 82, DESI Legacy, and HSC-SSP surveys, not all galaxies have complete coverage across all three datasets. Of the 838 galaxies in our final catalog, 539 have available HSC-SSP imaging, while 827 are covered in the DESI Legacy surveys.

Consequently, roughly 65% of the sample benefits from multi-survey data, which supports a more robust classification of galaxy structures.

For quantitative imaging analysis, we relied on the SDSS Stripe 82 data prepared by the IAC Legacy Project, which has been optimized to detect low-surface brightness features. To process and enhance these images, we used a semi-automated image analysis workflow — IMage ANalysis (IMAN)[2] — alongside additional Python-based scripts.

The initial processing steps involve cropping and rotating each image based on the galaxy center and position angle data from the SExtractor catalogs described in Fliri & Trujillo (2016). Upon visual inspection, we corrected the position angles for approximately 40% of the sample by fitting ellipses to the outer isophotes and recalculating their orientations. The cropping and rotation steps were then reapplied. Each galaxy cutout was standardized to a square with an angular side length equal to six times the semi-major axis (in arcsec) of the galaxy. These transformations were also applied to the corresponding error maps, which encode pixel-level photometric uncertainty.

Since the input images were already sky-subtracted, we did not perform an additional background correction. We used the *photutils* package[3] to generate masks for contaminating sources that are not related to the target galaxy. This processing was repeated for each photometric band, yielding coadded and rotated images (with the deep r band as the reference) and RGB composites that allow full exploitation of the depth and quality of the Stripe 82 data, especially in revealing extended low-surface brightness features surrounding the galaxies. A mosaic compiled of these co-added SDSS images for the ES82 sample is available online[4], with supplementary materials including additional image sets from the other survey datasets.

[2] https://bitbucket.org/mosenkov/iman_new/src/master/

[3] https://photutils.readthedocs.io/en/stable/

[4] https://physics.byu.edu/faculty/mosenkov/docs/Edge-on_Stripe82.pdf

3.1.3 Sample Completeness and the Catalog

To assess the completeness of our sample, we applied the V/V_m test as described by Thuan & Seitzer (1979). This method compares the volume V — calculated from the galaxy's distance $D = d/\theta$, where d is its linear diameter and θ its angular diameter — to the maximum volume V_m at which the galaxy would still meet the sample's angular size limit D_m. Here, $D_m = d/\theta_L$, with $\theta_L = 22.33$ arcsec, corresponding to the smallest Kron radius in the sample. The resulting volume ratio is $(\theta_L/\theta)^3$. A uniformly distributed, complete sample in Euclidean space should yield an average $\langle V/V_m \rangle$ of 0.5. By calculating V/V_m while progressively excluding galaxies with smaller angular sizes, we found that the sample is effectively complete for galaxies with $r_{\rm Kron} > 61$ arcsec (45% of the sample), yielding $\langle V/V_m \rangle = 0.49$ in the r-band. Although only 45% of our sample is complete, we did not exclude the other 55% from analysis or the catalog.

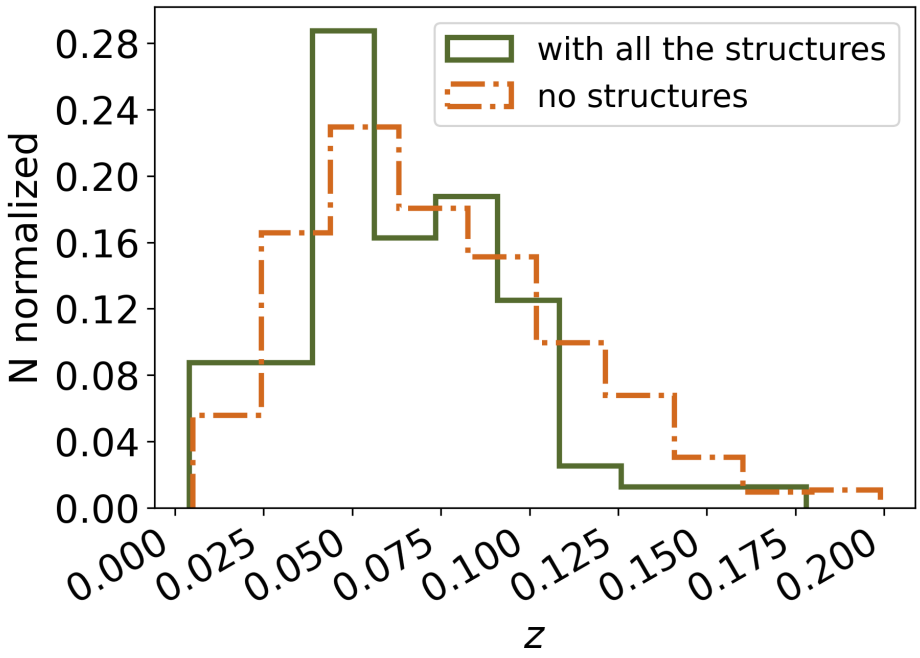

Figure 3.2 Redshift distribution for galaxies from the ES82 catalog with all tidal structures (49 galaxies) and those without (789 galaxies).

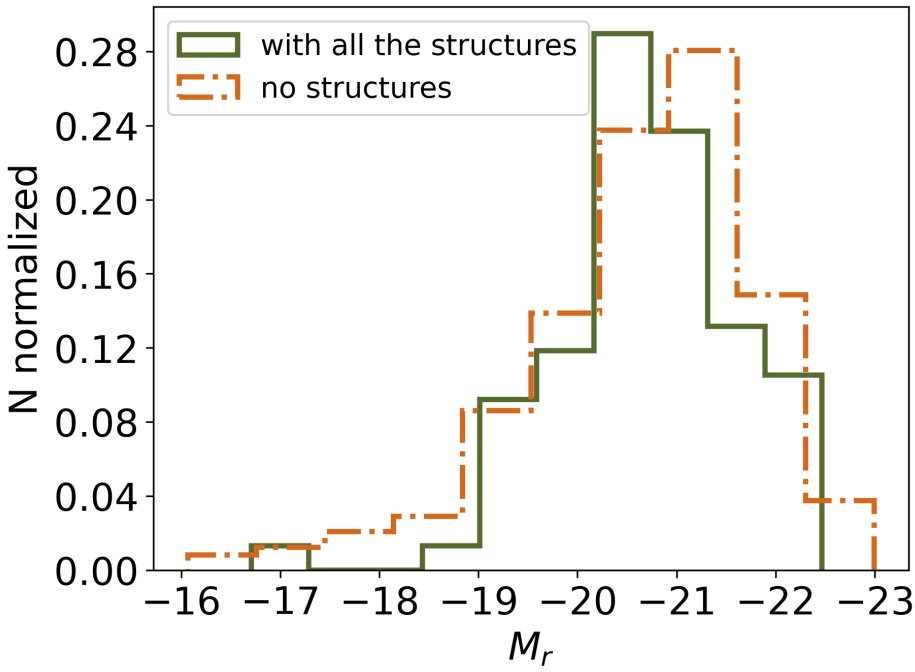

Figure 3.3 Absolute magnitude distribution for galaxies from the ES82 catalog with all tidal structures (49 galaxies) and those without (789 galaxies).

The full catalog is available in the online journal, including positions (R.A., Dec.), morphological parameters such as position angle (PA), axis ratio (q), the diskyness/boxyness parameter (C_0), redshift (z), and total r band magnitudes (taken from the SDSS best fit modeled magnitudes). The galaxies in the catalog cover a redshift range of $z = 0.004$ to $z = 0.2$, offering a representative sample well suited for identifying tidal structures. Fig. 3.2 displays the redshift distribution for galaxies with all the tidal structures and those without, both peaking at $z \simeq 0.06$, with quartiles of $0.06^{+0.03}_{-0.02}$. Fig. 3.3 displays that the catalog spans a typical range of absolute magnitudes for galaxies with all the tidal structures and for those without, with a median $M_r = -20.7^{+0.8}_{-0.7}$.

3.2 Structure Classification and Statistics

With such large data sets from modern sky surveys, using machine learning or automated parametric or non-parametric methods can help identify the morphology of galaxies (e.g. Kado-Fong et al. 2018, Sola et al. 2022) and possibly tidal features (Domínguez Sánchez et al. 2023). In addition, neural networks have identified cirrus clouds in deep optical images, including, in Stripe 82 (Smirnov et al. 2023). When it comes to galaxy LSB structures themselves, machine learning has not yet been trained to identify and separate them from Galactic cirrus, extended halos of bright, saturated stars, or image artifacts (especially artifacts of sky background subtraction). However, even with automated classification methods to identify LSB structures, studies still use human identification to ensure the avoidance of incorrect LSB structure candidates (Bílek et al. 2020; Martínez-Delgado et al. 2023; Mosenkov et al. 2024).

Therefore, we performed an LSB structure classification by visual inspection of images from the three independent deep surveys. Using four images, namely the stacked and color RGB images based on the SDSS Stripe 82, DESI Legacy, and HSC-SSP data, we reveal low surface brightness structures near some galaxies from the catalog. All the structures are divided into two categories: tidal structures and distinctive structural features described in chapter 2. Examples of tidal structures and distinctive structural features can be seen in Fig. 3.4 and Fig. 3.5.

In total, tidal structures and distinctive structural features are observed in 49 (5.8%) and 56 (6.7%) galaxies out of 838, respectively (taking into account Galactic cirrus by rejecting LSB features attributable to cirrus; see below). The type and frequency of the tidal structure are as follows:

1. Tidal tails and streams (15)

2. Diffuse shells (6)

3. Bridges (9)

4. Arcs (7)

5. Satellite debris (7)

6. Disk deformations (8)

In general, types of tidal structures are not limited to those listed above. These LSB structures are the most frequently encountered in this study (we refer the interested reader to, for example, Martínez-Delgado et al. 2010, Mancillas et al. 2019b, Sola et al. 2022).

The number of distinctive structural feature types are as follows:

1. Lopsided disks (11)

2. Warps (45)

3. Polar structures (3)

As discussed briefly at the beginning, if a galaxy is observed through the Milky Way's cirrus clouds or filaments, it can appear as if it has an LSB feature. To verify the results of our classification, we must ensure that the identified LSB features are not corrupted by Galactic cirrus. To aid in this, Smirnov et al. (2023) used SDSS Stripe 82 images to identify cirrus clouds with surface brightness < 29 mag arcsec^{-2} and produced a full cirrus map of the region using a neural network. Fig. 7.1 in the Appendix shows where our sample of galaxies is located along the cirrus map. Overall, we find that 72 galaxies in our entire catalog are within 3 times their radius of a cirrus filament or are directly contained within one. Of those 72 galaxies, 16 are directly contained within a cirrus filament. There are eight galaxies with tidal features that have cirrus filaments within close proximity, and upon inspection it was concluded that seven of those galaxies had minimal contamination and contained legitimate tidal features. In contrast, the galaxy ES82_2.265_-0.583 (an apparent tail), was highly contaminated and its effect could not be ruled out and therefore had to be removed as a tidal feature candidate. Overall, we find that cirrus has no appreciable effect on the results of our classifications.

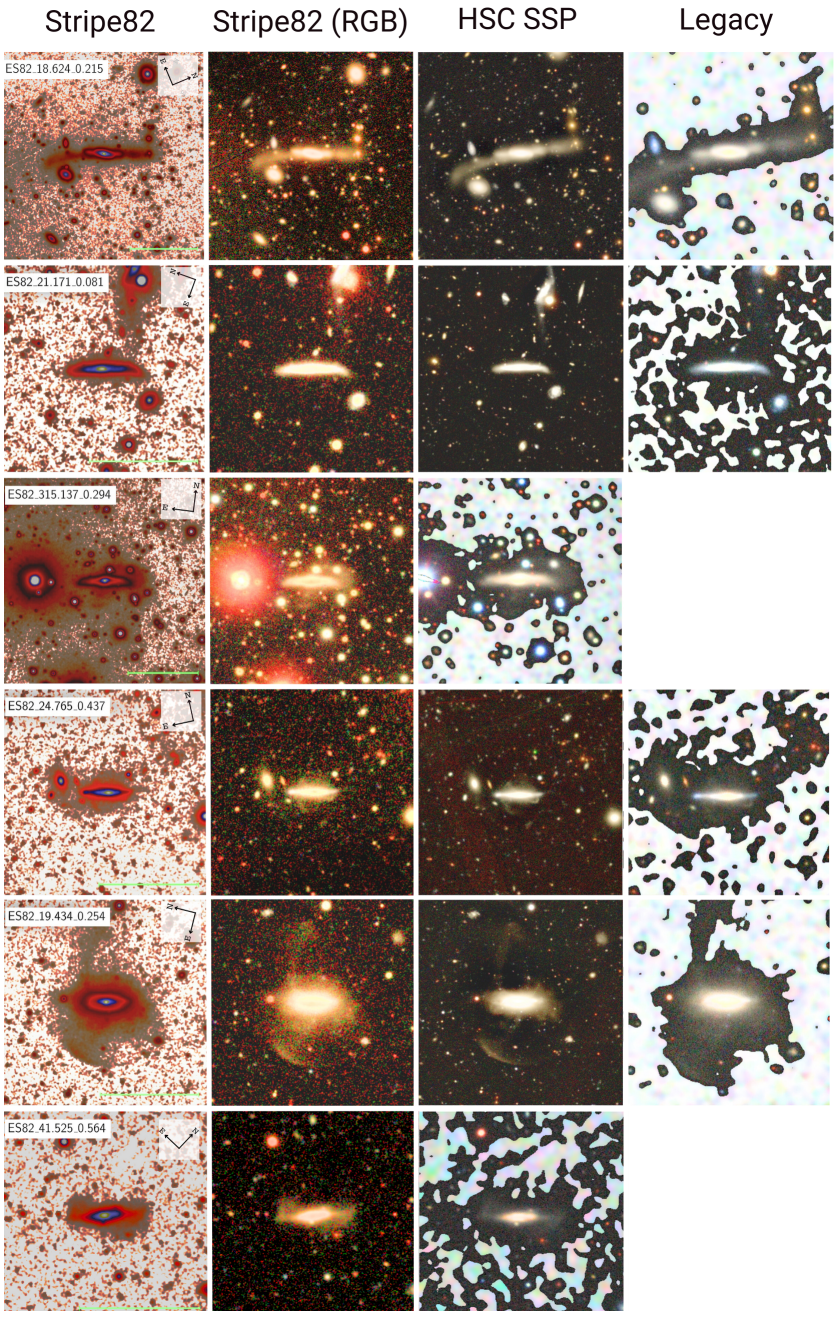

Figure 3.4 Examples of tidal structures observed in three independent surveys: the first two columns are SDSS Stripe 82 coadds and Stripe 82 RGB images (created using the g, r, and i bands), while the third and fourth columns are co-adds from HSC-SSP and DESI Legacy surveys, respectively. Each row demonstrates a galaxy with a tidal tail (top), a bridge, an arc structure, a satellite remnant, a shell, and a disk deformation (bottom). The scales of object images from different surveys may vary.

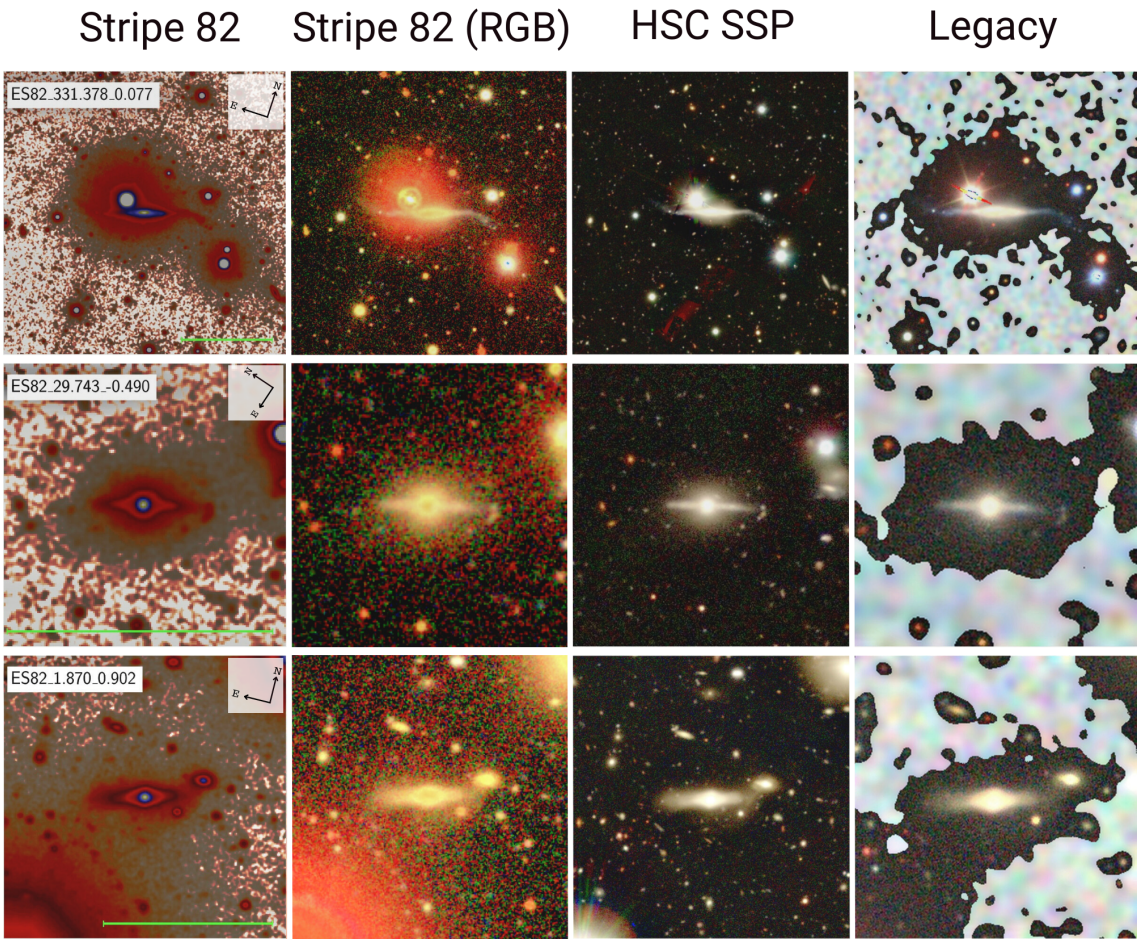

Figure 3.5 Examples of structural features observed in three independent surveys: the first two columns are Stripe 82 coadds and Stripe 82 RGB images, while the third and fourth columns are co-adds from HSC-SSP and DESI Legacy surveys, respectively. Each row demonstrates a galaxy with a warp (top), a polar-ring (middle), and a lopsided, distorted disk (bottom).

3.3 Summary and Conclusion for Stripe 82

In this chapter, we created a catalog of 838 edge-on galaxies in deep SDSS Stripe 82. Also, we identified and classified LSB and other distinctive structures near or in these galaxies based on data from three independent deep-sky surveys: SDSS Stripe 82, HSC-SSP DR3, and DESI Legacy Imaging Surveys DR9. For at least 65% of the galaxy sample, we have three different data sources for reliable structure classification. In the next chapter, we continue to investigate the statistics, structure, and surface brightness of LSB tidal and structural features around edge-on galaxies using a large sample size of almost 6,000 edge-on galaxies. The results of this and the next chapters will be compared and discussed in Chapter 5.

Chapter 4

The Atlas and Statistical Analysis of Galaxies from EGIS

This chapter presents the largest atlas and statistical analysis of features around edge-on galaxies ever conducted to date and will be compared to the Stripe 82 results presented in Chapter 3.

4.1 The EGIS Sample

Our sample consists of 5,745 true edge-on galaxies taken from the online catalog EGIS[1] (Edge-On Galaxies In SDSS) originally presented in Bizyaev et al. (2014), where a detailed explanation of how the galaxies were selected can be found. A summary will be given here. Candidate edge-on galaxies for the EGIS catalog were selected from the SDSS DR7 (Abazajian et al. 2009). After an initial visual inspection of the galaxy candidates to remove artifacts, the EGIS catalog was left with 14,983 galaxies. Further visual inspection for true-edge-on galaxies yielded 4,768 objects. To the initial sample, they also added genuine edge-on galaxies from the RFGC (Karachentsev et al. 1999), EFIGI (Baillard et al. 2011), RC3 (de Vaucouleurs et al. 1991) and GalaxyZoo (Lintott et al. 2011) surveys

[1]The catalog is publicly available here: EGIS

that were within the SDSS footprint, giving a total of 5,747 true edge-on galaxies (two galaxies were removed from our sample due to artifacts). Bizyaev et al. (2014) also conducted a simple automatic analysis of the structural parameters of the stellar disks in the g, r and i wavebands[2], where apparent magnitudes and morphologies were taken and used for later analysis. The inclination angles were also roughly estimated from the semi-minor over semi-major axis ratio (b/a) using equation $cos^2(i) = ((b/a)^2 - q^2)/(1 - q^2)$ (Hubble 1926), where $q = 0.13$ is the assumed intrinsic flatness of galaxy disks (Giovanelli et al. 1994). However, this approach introduced systematic uncertainties, as a single flatness value cannot accurately represent the intrinsic shapes of all galaxies. Consequently, this method was found to be less reliable than visual inspection for the selection of edge-on galaxies. Bizyaev et al. (2014) considered galaxies with inclination $> 86°$ as genuinely edge-on, but emphasized that visual classification remains more robust due to the limitations of using simplified geometric assumptions in the inclination estimation.

Bizyaev et al. (2014) found that the EGIS catalog is 95% complete (used the same method as presented in Section 3.1.3) for all galaxies with major axes angular sizes larger than 28 arcsec. The sample consists of galaxies with spectroscopic and photometric redshifts out to $z \approx 0.2$. Fig. 4.1 shows the spectroscopic redshift distribution for galaxies with and without tidal features. Both have similar distributions and peak at $z \approx 0.025$. The quartiles for both sub-samples are $z = 0.025^{+0.06}_{-0.03}$. Of the 5,745 galaxies in our sample, 4,837 (84%) have spectroscopic redshifts, while 429 (7.5%) have photometric but no spectroscopic redshifts, and 479 (8.3%) have no redshift data available. All redshift data, cross identifications, and galactic extinctions were collected from the NASA/IPAC Extragalactic Database (NED). All data for the 5,745 galaxies is compiled in a publicly available catalog called STAGE (**St**atistical **A**nalysis of **G**alaxies from **E**GIS). This catalog includes the right ascension and declination, the major and minor axes, central surface brightness, magnitudes for the g, r, and z bands, redshift, stellar mass, etc.

[2]The catalog is publicly available here VizieR

Similar to the Stripe 82 paper, we compared our SDSS sample to the DESI Legacy Imaging Survey (DR8, DR9, DR10) and the HSC-SSP (PDR2 and PDR3). This practice further enhances our classifications of tidal and other structural features by providing better-resolved and deeper images from the different surveys. For a detailed description of each survey, refer to Section 3.1.2. Additionally, we used the ARTIC instrument on the Apache Point Observatory (APO) ARC 3.5m telescope that is located in Sunspot, New Mexico, to take additional images for comparison. The ARTIC instrument has a field of view of 7.85 arcmin^2 with a pixel scale of 0.228 arcsec. Due to the limited time allotted to use APO, only 16 galaxies were imaged for the SDSS r and g bands (two galaxies were imaged only in the g band and one galaxy was only imaged in the r band). The average 3σ surface brightness limit reaches 29.4 ± 0.3 mag arcsec^{-2} in the g band and 29.0 ± 0.5 mag arcsec^{-2} in the r band in a 10×10 arcsec^2 region. Although the number of APO images is small, they remain scientifically valuable by offering insights into the most intriguing galaxies exhibiting tidal features that are not captured by the HSC-SSP. These images reach surface brightness depths that are higher than those of SDSS and the DESI Legacy Surveys, allowing for more confident identification of very faint tidal and structural features, and providing a robust validation of our conclusions.

The DESI DR10 has the most significant overlap with the EGIS sample, providing 5,605 galaxies in the g, r, i, and z bands. The average 3σ mag arcsec^{-2} surface brightness limit for these galaxies reaches 29.3 ± 0.2, 28.6 ± 0.2, 28.2 ± 0.3, and 27.7 ± 0.2 for the g, r, i, and z bands, respectively. The DESI and Stripe 82 r band surface brightness limits are the same and will be used later for comparison between the two catalogs. HSC-SSP provided us with 597 galaxies in the g, r, and i bands that match the EGIS sample. The average 3σ mag arcsec^{-2} surface brightness limits for the HSC-SSP for our sample reach 30.3 ± 0.4, 29.9 ± 0.3, and 29.6 ± 0.4 for g, r, and i bands, respectively. The SDSS images have an average surface brightness limit for the g, r, and i bands of 26.5 mag arcsec^{-2}.

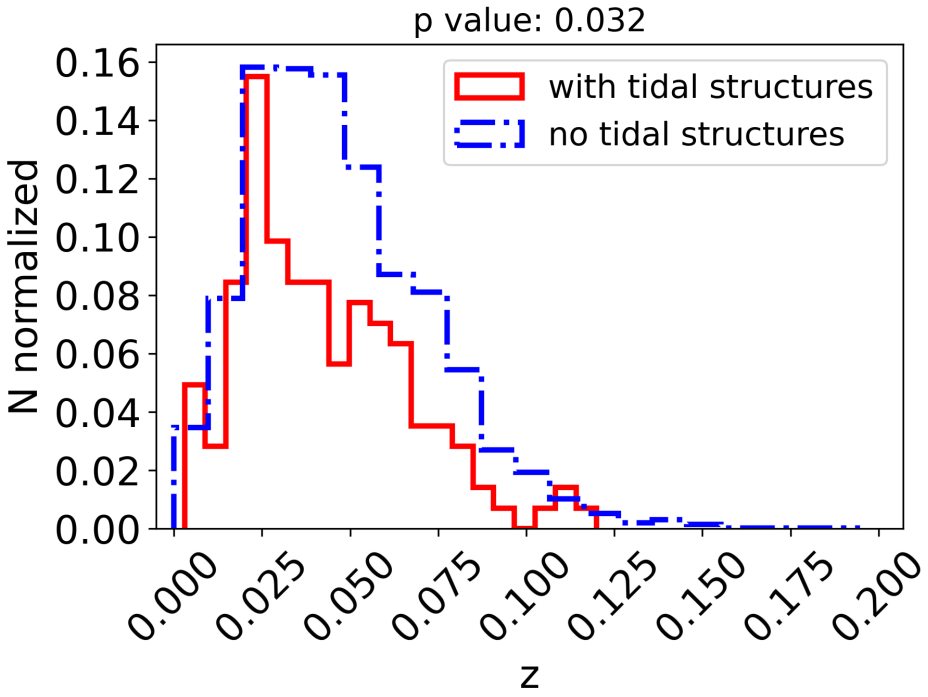

Figure 4.1 Spectroscopic redshift distribution for galaxies from the EGIS catalog.

4.1.1 Image Preparation

To classify the features in our sample, we prepared and processed FITS files from the SDSS, DESI Legacy, HSC-SSP, and APO for visual human classification. The process is described below.

The EGIS archive provides cutouts in the g, r, and i wavebands for all galaxies of the EGIS catalog. These FITS files are cropped based on isophotal boundaries where the signal-to-noise ratio per pixel drops to approximately 2, meaning that the outermost pixels included in the cutout are only marginally above the background noise. This results in a relatively small field of view that would limit the detection of faint features on the outskirts of the galaxies. Therefore, galaxy images were reprepared in the g, r, and i bands from the SDSS DR16 (York et al. 2000, Ahumada et al. 2020). Images were retrieved using a Python script[3] to download and concatenate adjacent fields

[3] https://github.com/latrop/sdss_downloader

from the SDSS archive. The subsequent image processing follows the same procedure described in Section 3.1.2.

DESI Legacy

A different approach was taken to process the DESI Legacy images for inspection. In the Stripe 82 paper, the DESI Legacy data were combined into RGB images after applying a Gaussian mask. We initially considered using this same method for our EGIS sample; however, due to the large number of galaxies in our sample, we wanted to make it easier to identify features within the images when viewed with a cursory glance to speed up the process of classification. Following Martinez-Delgado et al. (2021), we produced images that preserved the central RGB galaxy image while displaying a high contrast background to highlight faint structures. To do this, we wrote a custom pipeline in Python that first downloads the FITS files for each band, rotates the images using the position angle, and then crops the images to 6 times their semi-major axes angular size. It then masks out pixels that are below a surface brightness of 25 mag arcsec^{-2} and creates an elliptical mask for the galaxy using the semi-major and semi-minor axis values matching this threshold that are scaled by 1.2 and 1.3, respectively, to ensure that the galaxy is encompassed by the ellipse. Next, only the g, r, and i bands are stacked to be used as the background, as we found that this provides the deepest images (see Fig. 4.3). The stacked background image is then inverted, and a Gaussian blur is applied. The final step involves producing the galaxy's RGB image using code from the Legacy Sky Viewer[4], which is then overlaid on the stacked background. The final result for an example galaxy is shown in Fig. 4.2, alongside the corresponding RGB image and the RGB image with the Gaussian mask applied. From this comparison, we can see that our new method gives greater contrast to reveal structures. We visually inspected the images and eliminated any with large artifacts or missing data, which resulted in 5,606 processed images.

[4]Link will take you to exact line of code: Legacy Sky Viewer Code

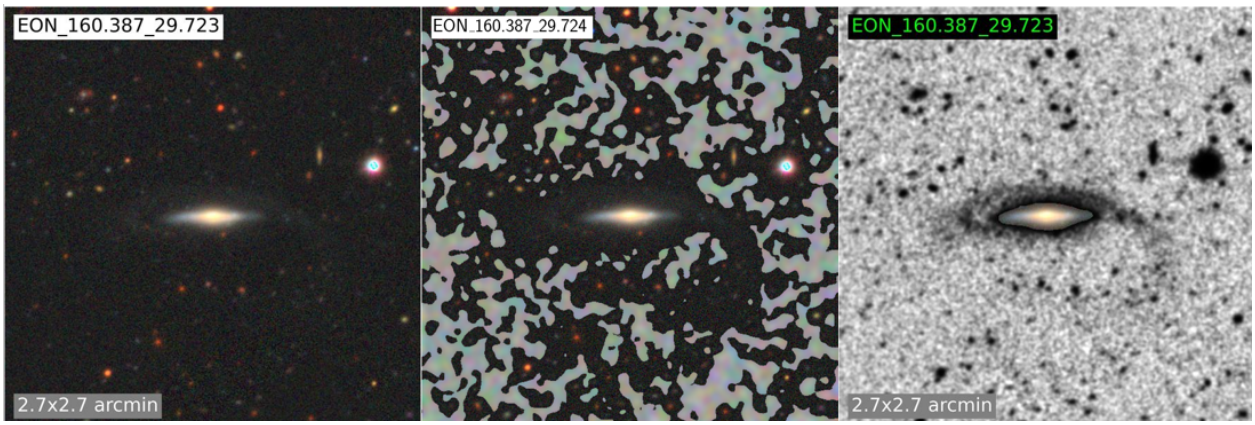

Figure 4.2 Comparison of different methods of processing images for the same galaxy. The image on the left is an RGB image. The middle image uses the Gaussian mask. The right image follows the method of Martinez-Delgado et al. (2021).

Unfortunately, only 2,261 *i* band images were usable for stacking, after removing those affected by artifacts or missing data. Because the *i* band contributes significantly to the depth of the stacked background, we specifically note in the Atlas which galaxies include the *i* band FITS file in the background. Full RGB images were also generated for inclusion in the Atlas as reference visuals. For galaxies in the EGIS sample that do not overlap with the DESI footprint, RGB images were instead created using SDSS data to ensure full sample coverage.

HSC-SSP

The same method was used for the DESI images as for the HSC-SSP images. We utilized code provided by the HSC-SSP survey to download g, r, and i band FITS files to create RGB images and incorporated the code into our pipeline. After processing the images downloaded from the PDR3, it was discovered that a large portion of the images have an over-aggressive background sky subtraction, leading to partial obscuration of the galaxy and its outskirts. It was concluded that the process of fixing sky subtraction would be too time consuming, and we sought to mitigate the effects by downloading images from the PDR2, as the images from the PDR2 had better sky subtraction.

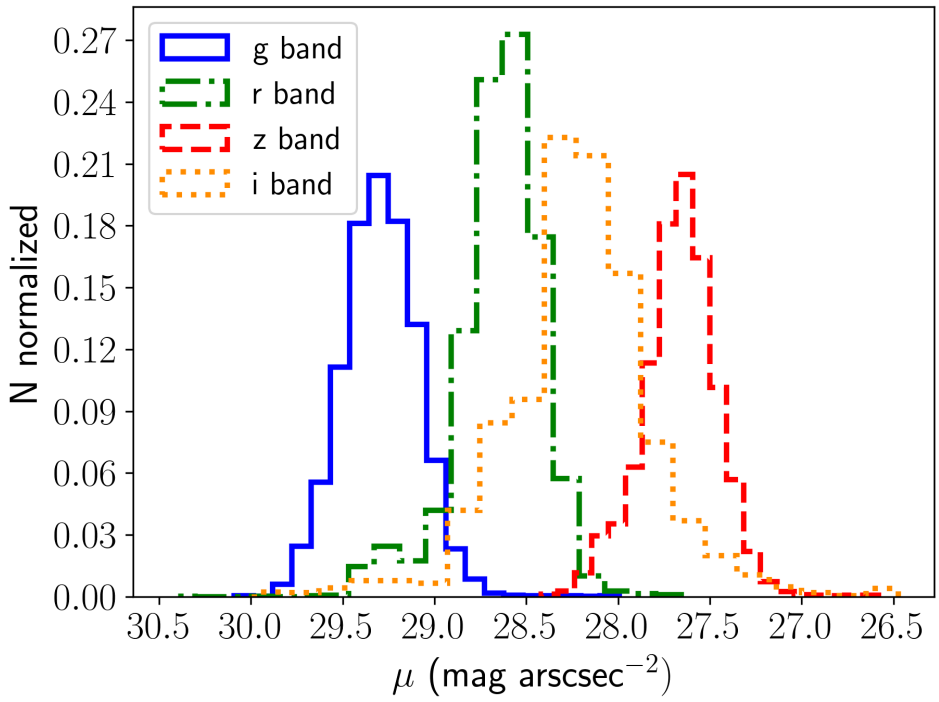

Figure 4.3 Surface brightness limit distribution for all bands in our DESI Legacy images that are in the EGIS catalog.

Not all the images from the PDR2 were worth keeping, and so the HSC-SSP image sample has a mixture of PDR2 and PDR3 images. After eliminating images with large artifacts, missing data, and over-sky subtraction, we were left with 597 HSC-SSP images.

APO

While the APO 3.5m telescope observations do not significantly contribute to the statistically complete EGIS catalog, they offer valuable insight into how deeper imaging can enhance the detection and characterization of faint structures as discussed earlier in Chapter 1 (see Fig. 1.1). Galaxies selected for APO observations were chosen because they exhibited potential faint structures (as discussed in Chapter 2) that appeared ambiguous or only marginally detectable in surveys like SDSS and DESI — see also a recent study on the edge-on galaxy UGC 10043 (Bahr & Mosenkov 2025). The APO images reinforce that the photometric depth strongly impacts the detection and

identification of LSB structures. To date, 25 galaxies have been observed, with 16 overlapping with the EGIS sample. Observational information for each galaxy can be seen in Table 4.1. The images were only taken in the *g* and *r* bands. Using a pipeline from IMAN, the raw FITS files were reduced and then processed as previously described for DESI and HSC-SSP images. All APO images can be seen in Fig. 7.2, Fig. 7.3, and Fig. 7.4. Because the APO images only have two bands, DESI images were used to create the color galaxy overlay.

4.2 Data

A study of LSB and other structural features was carried out, following a similar methodology to the Stripe 82 paper. Galaxies were classified using visual inspection across three surveys: SDSS, DESI, and HSC-SSP. A combination of experienced researchers and trained student classifiers participated in the process. For this study, expert classifiers are defined as individuals with several years of experience identifying galactic structures, who have published work in the field and have been involved in training others in classification techniques. In contrast, student classifiers, while trained for this project, had limited prior experience and were still in the process of developing the expertise required for high-confidence identifications. Classifiers were asked to vote on whether a galaxy exhibited a particular feature. The number of affirmative votes was divided by the total number of classifiers to produce a confidence percentage for each feature. Using a similar method as in Simmons et al. (2017), "Maybe" was assigned to a feature with voting reaching 30% < x < 50%, "Good" was assigned to 50% < x < 70%, and "Best" was assigned to 70% < x < 100%. The expert classifiers then reviewed all classifications again and revised those that were erroneous to ensure accuracy. It was found that a large portion of warped and lopsided galaxies were incorrectly identified in the initial phase of classification, as these types of structures are more prone to visual bias. Small variations in the disk's length or deviations from the mid-plane can be difficult to discern

Table 4.1 Observational information of galaxy images from the APO.

Name	Date *g*	Date *r*	Time × N *g*	Time × N *r*	FWHM *g*	FWHM *r*
EON_5.686_14.950	10/12/2023	10/12/2023	900x5	900x4	2.2±0.1	1.2±0.0
EON_9.910_14.664	10/12/2023	10/12/2023	900x5	900x4	2.2±0.1	1.7±0.3
EON_46.480_-8.019	1/3/2024	10/12/2023	900x4	900x5	2.4±0.4	2.8±0.2
EON_117.934_42.253	N/A	1/3/2024	N/A	900x4	N/A	2.4±0.1
EON_137.491_43.851	2/28/2022	2/28/2022	900x5	900x5	1.4±0.1	1.8±0.4
EON_146.725_23.023	N/A	11/15/2023	N/A	900x4	N/A	1.7±0.6
EON_148.062_47.076	3/25/2022	3/25/2022	900x5	900x5	1.3±0.2	1.7±0.2
EON_164.403_44.071	3/25/2022	3/25/2022	900x5	900x5	2.0±0.3	2.0±0.1
EON_184.615_12.696	5/5/2022	5/5/2022	900x5	900x5	2.0±0.1	1.9±0.1
EON_191.925_26.982	3/28/2022	3/28/2022	900x5	900x5	1.3±0.3	1.4±0.3
EON_201.959_40.080	5/5/2022	5/5/2022	900x5	900x5	1.8±0.1	1.6±0.0
EON_210.947_35.742	3/28/2022	3/28/2022	900x5	900x5	1.1±0.1	1.3±0.0
EON_223.968_24.720	6/10/2024	N/A	900x4	N/A	1.6±0.1	N/A
EON_235.731_9.228	5/5/2022	5/5/2022	900x5	900x5	1.8±0.2	2.0±0.1
EON_237.173_21.870	4/12/2024	4/12/2024	900x5	900x5	2.2±0.1	1.8±0.2
EON_330.124_11.380	5/5/2022	5/5/2022	900x5	900x5	1.4±0.3	1.2±0.3

Notes: Observational details for the 16 galaxies imaged with the APO. Some galaxies were observed only in one of the bands. The first column lists the galaxy names as given in the EGIS catalog. The second and third columns indicate the observation dates for each band. The fourth and fifth columns provide the exposure time (in seconds) and the number of exposures. The sixth and seventh columns list the FWHM values for the target galaxy in each band, measured in arcsec.

with the human eye. This prompted an investigation into a more automatic and accurate approach to identifying these types of galaxies. Section 4.2.3 discusses in greater detail this process and the data collected.

4.2.1 The Atlas

In the spirit of Stripe 82's multi-survey presentation of galaxy images, we present a comprehensive atlas that integrates data from multiple surveys to provide a detailed visual and quantitative record of each galaxy in our sample. This EGIS Atlas serves as the primary outcome of this study, offering a valuable resource for future investigations of edge-on galaxy morphology, tidal features, and environmental effects. Each page of the atlas features a reference RGB image, primarily from DESI Legacy. For the 139 cases where DESI images were unavailable, SDSS RGB images were used in their stead. The atlas compiles key information for each object, including processed survey images, tidal and structural classifications, edge-on morphological assessments, Galactic cirrus contamination classifications, and relevant annotations. Supplementary data such as cross-identifications, equatorial coordinates (in both sexagesimal and decimal degrees), redshift, and redshift quality flags from NED are also provided. An example page from the EGIS Atlas is shown in Fig. 7.8.

4.2.2 Structure Classifications

We use the same tidal and structure classifications as for the Stripe 82 sample, only excluding the "Disk Deformation" tidal classification as it is redundant and could be included with the "Diffuse Shells, Plumes, or Asymmetric Stellar Halos" classification when only considering the deformed or distorted stellar disks. All classifications can be found in the Atlas with their corresponding galaxy.

When including all confidence levels (Maybe, Good, and Best), tidal structures are observed in 236 galaxies out of 5,745 (4.1%), while the highest confidence (Good and Best) subset of tidal

structures are observed in 159 galaxies (2.8%) after taking into account galactic cirrus as described in Section 4.2.4. Examples of the tidal structures classified in this sample are shown in Figs. 7.5 and 7.6. The total number of structures for the highest confidence subset is presented below. Note that this count includes multiple features per galaxy; therefore, the total number of structures exceeds the number of galaxies with tidal features and for structural features:

1. Tidal tails and streams: 72
2. Diffuse shells: 36
3. Bridges: 17
4. Arcs: 46
5. Satellite debris: 12

Using only visual inspection and including all confidence levels, structural features are observed in 1,229 galaxies (21.4%), while the highest-confidence subset of structural features is observed in 841 galaxies (14.6%). Examples of structural features classified in this sample are shown in Fig. 7.7. The total numbers of structural features for the highest confidence subset are presented below:

1. Lopsided disks: 200
2. Warps: 636
3. Polar structures: 52

4.2.3 Warped and Lopsided Galaxies

As discussed above, visually classifying warped and lopsided galaxies does not yield accurate results, as some warps and lopsidedness can escape human detection. Therefore, we employed an automatic

and semi-automatic method for their detection. Stacked g and r band FITS images were used for this analysis, as they provide the best view of faint optical warps and extended disks. The automatic method uses a Python script to create isophotes around each galaxy at surface brightness levels of 24 and 26 mag arcsec^{-2}, providing insight into the internal and outer structure of each galaxy (these specific values were selected after careful visual inspection of 100 galaxies with varying isophote levels). It then takes vertical slices along the major axis of each galaxy and fits a sech^2 profile to find the endpoints of the centerline of the isophotes. The distance from the endpoints to the center of the galaxy is determined and then used to calculate the angles and lopsidedness for each isophote. This process was successfully used for 90% of our sample. The remaining 10% have bright objects near the galaxy's disk, causing errors in the results.

The semi-automatic approach was developed for analyzing the remaining 10%. This approach uses a Graphical User Interface (GUI), utilizing the Python package matplotlib to visualize the galaxies and their isophotes. The GUI allows the user to directly select where they believe the edge points of the isophotes are by double-clicking to ensure no accidental selection. Additionally, the GUI provides various tools to ensure accurate selection and measurements. One button allows the user to change their selection of the edge points. Another button allows them to change the center point from which the angles and lopsidedness are calculated, in the case that the galaxy is not properly centered. Central isophotes are plotted that range from 21–22.5 mag arcsec^{-2} in 0.5 mag arcsec^{-2} increments to act as a guide to help determine if the galaxy is properly oriented and centered. Furthermore, the user can change the strength of the Gaussian smoothing to better estimate the isophotes and can also rotate the entire image for better alignment. An example of the GUI can be seen in Fig. 4.4.

The analysis of the results from the inner 24 mag arcsec^{-2} isophote is outside the scope of this thesis, but will be studied in more detail in a related paper to give more insight into internal warps and lopsidedness. We use the outer 26 mag arcsec^{-2} isophote values for our classifications and

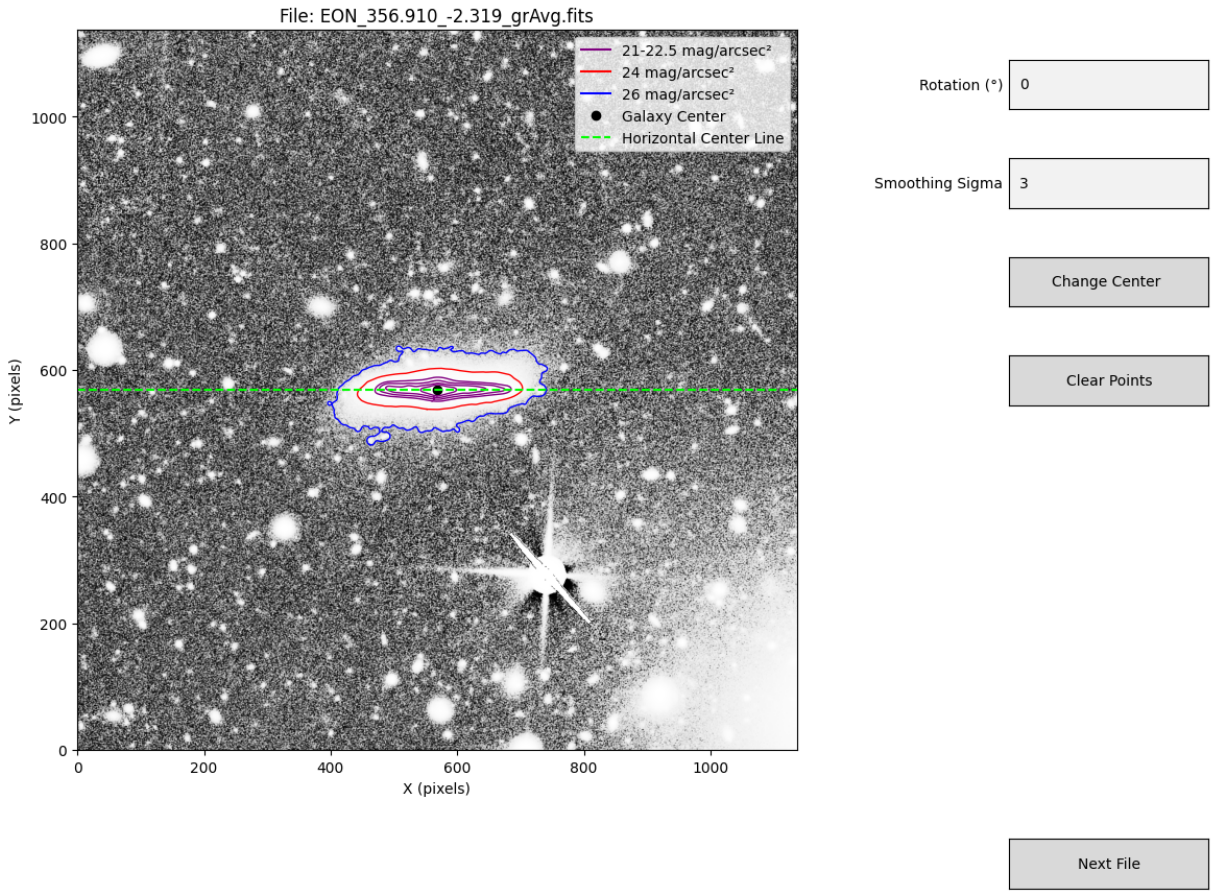

Figure 4.4 An example of the semi-automatic warp and lopsided GUI that gives the user different options to ensure accurate measurements. The lime green dashed line helps the user to ensure the galaxy is correctly oriented when compared with the central purple isophotes that range from 21–22.5 mag arcsec^{-2} in 0.5 mag arcsec^{-2} increments.

analysis as these best represent the visible structures' radial distribution. Lopsidedness for this study is defined as the absolute value of the difference between the left and right radii divided by the smallest radius. We adopt a threshold of $\geq 3°$ to consider a disk warped. This is consistent with other studies (Reshetnikov & Combes 1998, Sánchez-Saavedra et al. 2003, Reshetnikov et al. 2025). As for the threshold for lopsidedness, numerous studies use a lopsidedness value ≥ 0.10 (Bournaud et al. 2005, van Eymeren et al. 2011, Łokas 2022, Varela-Lavin et al. 2023). Using these thresholds and a sigma clip of 3σ to eliminate possible false detections, we find that 2,458 galaxies (42.8%)

Table 4.2 Statistical information for warped and lopsided galaxies.

Parameters	S-type	U-type	Lopsided
Incidence	409	2049	1965
Number Fraction	7.1%	35.6%	34.2%
Median Warp Angle	$4.83° \pm 1.71°$	$4.39° \pm 1.50°$	N/A
Median Lopsidedness	N/A	N/A	0.16±0.07
Median Mass $Log_{10}(M_\star/M_\odot)$	10.66±0.45	10.55±0.54	10.42±0.59

Notes: The number of galaxies, fractions, and median values are provided for warped and lopsided galaxies.

exhibit warps, while 1,965 galaxies (34.2%) exhibit lopsidedness, showing a significant increase when compared with those that were visually classified.

We separate the warped galaxies into two categories, S- and U-type warped galaxies, based on the orientation of the warped features. In S-type galaxies, the warps bend in opposite directions, whereas in U-type galaxies, the warps bend in the same direction, following the conventional classification scheme (Reshetnikov & Combes 1998, Ann & Park 2006, Reshetnikov et al. 2025). A total of 409 S-type and 2049 U-type galaxies are identified, as summarized in Table 4.2, along with additional statistical properties. Zee et al. (2022) analyzed a sample of approximately 8000 edge-on galaxies from SDSS, selected over a comparable stellar mass and redshift range, and reported a warp fraction of 48.5%, in good agreement with our value of 42.8% and consistent with those of previous studies that approach or exceed 50% (Sánchez-Saavedra et al. 1990, Ann & Bae 2016, García de la Cruz et al. 2023). Our median values also agree within the reported uncertainties. However, a notable discrepancy arises in the number fraction of S-type warps: while Zee et al. (2022) find S-types to be the most frequent (27.6% of their warped sample), we observe a significantly lower fraction of 7.1%, making them the least common in our dataset. Other studies similarly report

S-types as the dominant warp type (Ann & Park 2006, Ann & Bae 2016, Zee et al. 2022, García de la Cruz et al. 2023, Reshetnikov et al. 2025), further highlighting this discrepancy. This discrepancy is unlikely to stem from differences in sample selection, as our dataset closely matches the morphology, redshift, and stellar mass distribution of the sample used by Zee et al. (2022). Instead, it may arise from differences in the measurement methodology. Unlike other studies' approaches, which employ Fourier analysis of the light distribution to quantify warp orientation, our method relies on direct geometric measurements without such decomposition. Additionally, we did not mask out bright sources near the target galaxies, which may have introduced noise or asymmetries that affected the classification of S- and U-type warps. These potential sources of bias will be explored further in a forthcoming study.

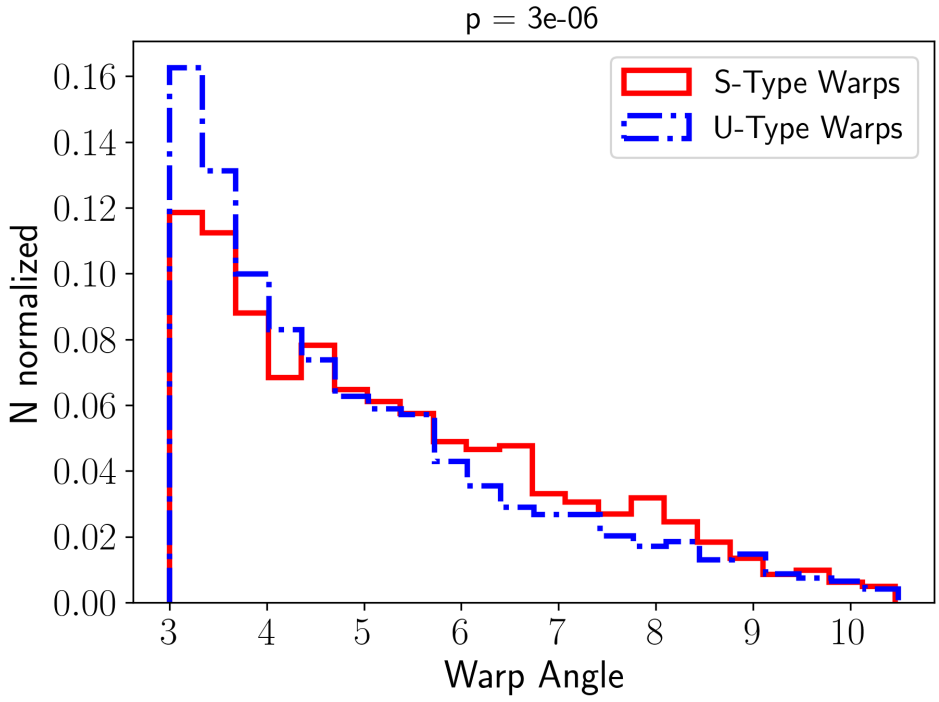

Figure 4.5 Distribution of warp angles for S- and U-type warped galaxies from the EGIS sample using the data from the 26 mag arcsec^{-2} isophote. A low p-value is obtained for the null hypothesis that both distributions are the same.

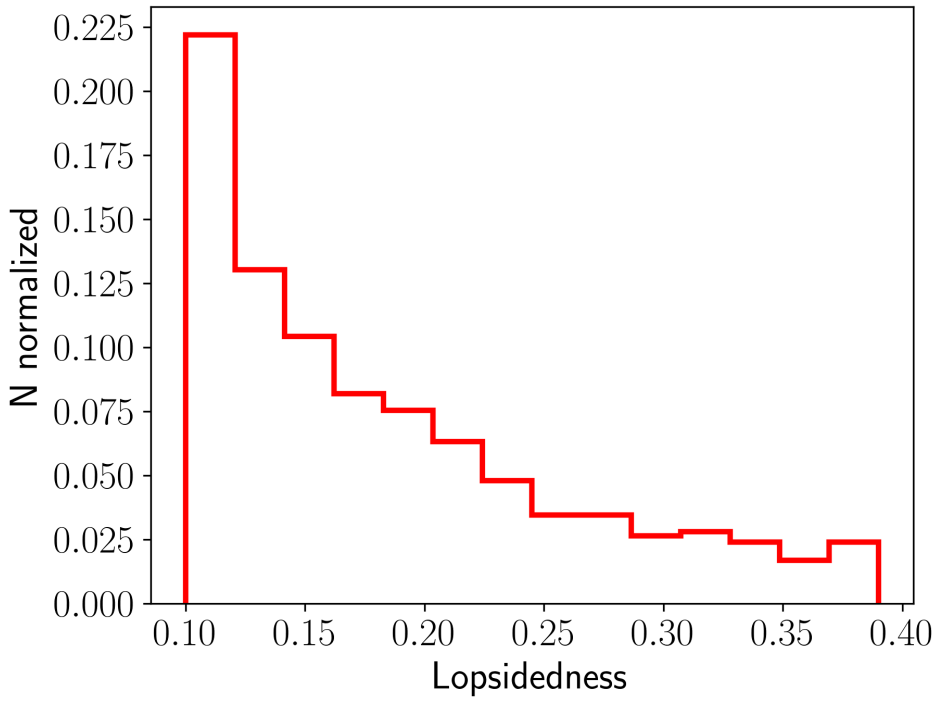

Figure 4.6 Distribution of lopsidedness for galaxies from the EGIS sample.

As shown in Fig. 4.5, the distributions of warp angles for both S-type and U-type galaxies are broadly similar, with both peaking at ~3.2°. To assess whether the two distributions are statistically distinct, we performed a Mann–Whitney U test to evaluate the null hypothesis that the S-type and U-type warp angle samples are drawn from the same underlying distribution. The resulting p-value of 3×10^{-6} allows us to reject the null hypothesis with high confidence, indicating that the distributions are significantly different. A closer inspection of Fig. 4.5 reveals that S-type warps exhibit a slightly higher frequency of larger warp angles compared to U-types, a trend also reflected in the difference in median values and is consistent with the findings of Zee et al. (2022). In addition to warps, we also examine the distribution of lopsidedness, shown in Fig. 4.6, which peaks at a value of 0.11. Previous studies report that approximately 30% of galaxies exhibit lopsidedness > 0.10, in good agreement with our measured fraction of 34.2% (Bournaud et al. 2005, Jog & Combes 2009).

4.2.4 Galactic Cirrus

To properly account for Galactic cirrus clouds that may interfere with our tidal classifications, we conducted a visual inspection of all 5,745 fields from the EGIS catalog, specifically searching for signs of optical Galactic cirrus contamination. For candidate fields showing potential signs of contamination, we used the Legacy Survey Sky Browser with viewer settings—contrast set to 1.2 and brightness to 7.5 — to ensure no false detections of cirrus due to artifacts. Using this method, we identified 547 (9.5%) fields or galaxies with optical Galactic cirrus contamination, defined as cirrus overlapping the galaxy or located within an angular distance comparable to the galaxy's radius. Each identified cloud was qualitatively classified by relative brightness (see Fig. 4.7): 339 were classified as dim, 149 as moderate, and 60 as bright. During this process, each field was re-checked to reinforce the reliability of our final selections. Of the 547 galaxies with neighboring cirrus, 11 exhibit tidal features. Upon visual inspection, we concluded that all 11 have minimal contamination and contain genuine tidal structures. Therefore, similar to the Stripe 82 results, we find that cirrus has no appreciable effect on our classifications.

Figure 4.7 Examples of Galactic cirrus with relative brightness of dim (left), moderate (middle), and bright (right).

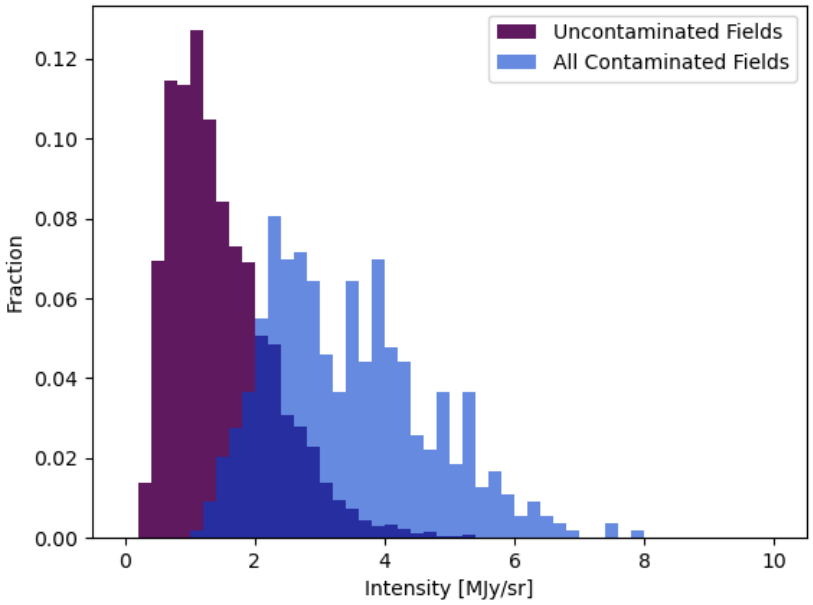

Figure 4.8 A comparison between IR intensity for galaxies with and without optical Galactic cirrus contamination.

To further characterize these contaminated fields, we estimated the corresponding infrared (IR) intensity near each galaxy using the IRAS (Infrared Astronomical Satellite) Infrared Maps[5] at a wavelength of 100 µm (Miville-Deschênes & Lagache 2005). For each object, we used its sky coordinates to locate its position on an IR sky map and calculated the average IR intensity from the eight surrounding pixels. Fig. 4.8 compares the IR intensity distributions of fields with and without optical cirrus contamination. As expected, contaminated fields exhibit, on average, systematically higher IR intensities associated with the greater cold dust emission. Despite this trend, the overlap between the two distributions remains substantial. In principle, one would expect a clear separation between the two populations, since cirrus contamination should correspond to elevated IR emission due to thermal radiation from dust grains heated by the interstellar radiation field.

[5] https://lambda.gsfc.nasa.gov/product/iras/iras_iris_get.html

The presence of overlap may be attributed to several factors. First, optical and infrared cirrus do not always correlate directly, as they probe different physical processes and dust properties. Optical cirri are visible due to scattering and depend on the geometry of the illumination and the grain properties, while infrared cirri are detected via thermal emission, which is sensitive to dust temperature and emissivity. As a result, some regions may appear bright in one band but faint or even undetectable in the other. Additionally, differences in spatial resolution, depth, and sensitivity between the optical and infrared datasets can further obscure the correspondence between cirrus detections in the two regimes (Ienaka et al. 2013, Seon & Witt 2013, Román et al. 2020, Marchuk et al. 2021, Smirnov et al. 2023). These effects likely contribute to residual IR cirrus emission in fields classified as uncontaminated in the optical, thereby producing the observed overlap and limiting the reliability of IR intensity alone as a discriminant for cirrus contamination.

Chapter 5

Discussion of Results

The results presented in Section 3.2, which include the classification and statistical analysis of LSB and other distinctive features, show that the ES82 catalog contains a lower fraction of galaxies with tidal structures than predicted by galaxy formation models within the standard ΛCDM cosmological framework (Johnston et al. 2001, Martin et al. 2022). To address this, we expanded our analysis to include the larger and more complete EGIS catalog. We chose this approach because many previous studies of tidal features rely on relatively small samples, which limits their ability to capture the true frequency and diversity of such structures. By leveraging the broader coverage of the EGIS catalog, we aimed to obtain a more representative picture of the tidal feature population. However, our findings in Section 4.2 show that even within this larger dataset, the fraction of galaxies exhibiting tidal structures remains low, which is consistent with our Stripe 82 results.

Interacting galaxies are a common phenomenon in the local Universe, as evidenced even by our own Galaxy (Putman et al. 1998, Lee et al. 1999, Belokurov et al. 2006). Cosmological simulations within the standard ΛCDM model predict that a significant number of coherent tidal structures may be detected with sufficiently deep observations in the outskirts of the majority of nearby massive galaxies (Font et al. 2011, Cooper et al. 2013, Pillepich et al. 2015). Johnston et al. (2001) consider ∼100 parent galaxies and find 20–40% (see Fig. 5.1) of galaxies should demonstrate tidal features

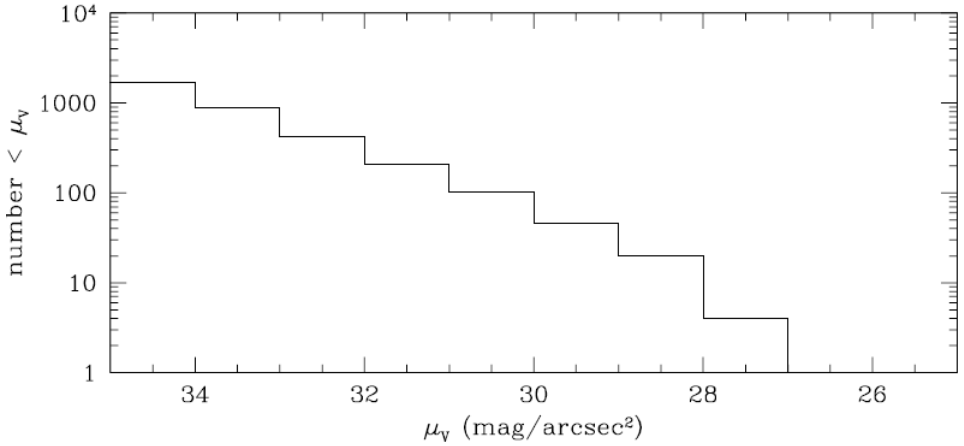

Figure 5.1 Figure 8 from Johnston et al. (2001), which shows the total number of features estimated below a given limiting surface brightness.

when reaching a surface brightness limit ∼29 mag arcsec^{-2}. In a recent study, in preparation for the 10-year Legacy Survey of Space and Time (LSST) at the Vera C. Rubin Observatory, Martin et al. (2022) demonstrated the ability to detect tidal features using the NEWHORIZONS cosmological simulation (Dubois et al. 2021). As shown in Fig. 5.2, varying the limiting surface brightness in the *r* band (28–31 mag arcsec^{-2}) affects the detection of tidal features across different redshifts. Using this figure and the mean redshift of our samples, we find that at a limiting surface brightness of 28 mag arcsec^{-2} in the *r* band, approximately 25% and 30% of our sample from Stripe 82 and EGIS, respectively, should exhibit tidal features. Furthermore, Valenzuela & Remus (2022) utilized the Magneticum simulation to measure a tidal feature fraction of 23%, which is only 2% lower than that found by Martin et al. (2022). This comparison further demonstrates the insufficient number of galaxies with tidal features in both our samples compared to those predicted by cosmological simulations.

However, a recent study by Miro-Carretero et al. (2024) presents results that align more closely with our findings, reporting a predicted tidal feature fraction of ∼ 7% (see Fig. 5.3) at a limiting surface brightness of 28.6 mag,arcsec^{-2} in the *r* band, comparable to the depth of our observations. In their analysis, mock images generated from three cosmological simulations — Copernicus

Complexio (COCO), Illustris TNG50, and Auriga — were examined across a range of surface brightness thresholds in the *r* band to assess the visibility of tidal features. They found that the predictions from the TNG50 and Auriga simulations were in good agreement with observed tidal fractions, while the COCO simulation overestimated the number of detectable features. They mention that this could be because COCO uses particle tagging models, which can lead to increased tidal fractions. However, it is important to note that this study is currently available as a preprint and has not yet completed the peer review process. As such, while its results offer valuable context, they are treated here as preliminary and are not included as central evidence in our discussion.

We further seek to compare our results with those in the literature. It is important to note that none of the studies discussed below use the same method as that used in this study to calculate the limiting photometric depth. Given the substantial differences in methodology, recalibrating

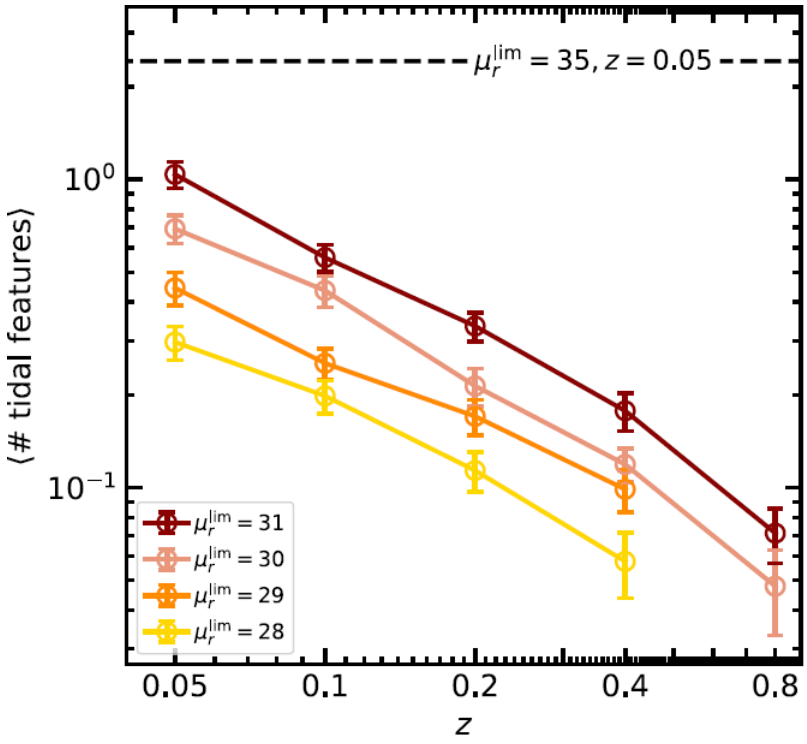

Figure 5.2 Figure 17 from Martin et al. (2022), which shows the total number of features estimated across different redshifts for a specific limiting surface brightness.

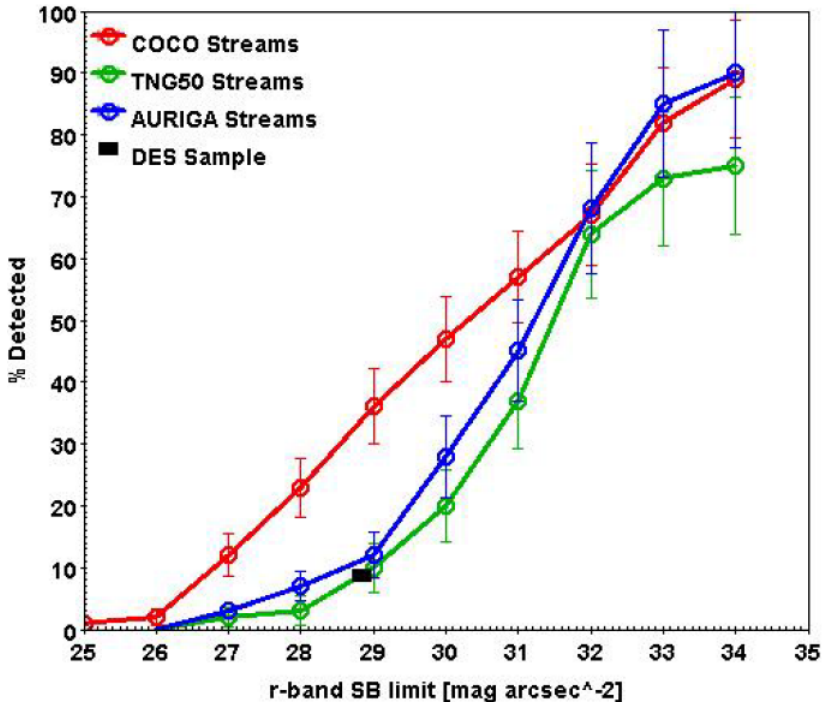

Figure 5.3 Figure 11 from Miro-Carretero et al. (2024), which shows detection rate curves across different limiting surface brightness for the COCO, Illustris TNG50, and Auriga cosmological simulations.

the limiting surface brightness of our sample to align with those of the cited studies would require an extensive, time-intensive recalibration process. Consequently, such recalibration was deemed impractical and was not undertaken. In an observational study using HSC-SSP data, Kado-Fong et al. (2018) found tidal features in 1,201 out of 21,208 sample galaxies (5.6%). This is consistent with our complete data sets, defined as galaxies with $R_{Kron} > 61$ arcsec for Stripe 82 and major axes > 28 arcsec for EGIS, in which we confirmed tidal structures in 26 galaxies out of 374 galaxies (7%) and 159 out of 5,745 galaxies (2.8%), respectively. However, Kado-Fong et al. (2018) does not explicitly state whether their sample is complete at the reported surface brightness limit of $\mu_r = 28.1$ mag,arcsec^{-2}. For our incomplete data set (galaxies with $R_{Kron} < 61$ arcsec) in Stripe 82, the presence of tidal features has a ratio of 24 galaxies out of 464 galaxies (5.2%). Kado-Fong et al. (2018) used various methods obtained from the literature (see references therein) to calculate the

limiting depth of their sample, but none of these methods match with ours. Morales et al. (2018) found tidal features around $\sim 10\%$ of a mass-selected sample of isolated Milky Way analogues at a limiting surface brightness of 28 mag arcsec^{-2}. Their sample is considered mass-complete above a stellar mass threshold of $10^{9.2}$ $M_{\odot}$, meaning that all galaxies above this limit were included within the selected volume. To estimate the depth of their study, Morales et al. (2018) used 5σ fluctuations within 3 arcsec diameter apertures.

There could be numerous reasons why our statistics do not match with other observations and simulations. Reasons such as visual bias, projection effects, redshift and mass selection biases, insufficient image depth, contamination by Galactic cirrus clouds, and the reliability of cosmological hydrodynamic simulations can all play a role. Below, we briefly consider all of these.

5.1 Visual Bias

As noted above, visual classification was used to categorize the types of tidal and structural features within our sample. However, visual analysis can be subjective, depending on the individual classifier, and can lead to disagreements among different classifiers (Bridge et al. 2010, Blumenthal et al. 2020). For example, Martin et al. (2022) used five experienced classifiers to categorize tidal features in mock images, with some classifiers marking an image as having a feature, while others marking it as featureless. When reviewing the images again, many revised their original answers. This shows that even experienced classifiers can be uncertain and that classifications should be revisited numerous times to ensure accuracy. In the case of the Stripe 82 and EGIS samples, some galaxy images might have been overlooked and not identified as having tidal features. For this reason, the entirety of both catalogs was examined by several classifiers to mitigate subjectiveness, but it is still difficult to estimate the extent to which this has impacted our classification results. Bridge et al. (2010) conducted a blind study and found that classifications varied only 3% of the time between

classifiers. We take this percentage as a lower estimate for our classifications. Another method used to help eliminate visual bias is the method of applying weights to different classifiers and their classifications. Citizen science projects such as Galaxy Zoo and Galaxy Cruise use this method with great success, assigning greater weight to the most consistent classifications (Simmons et al. 2017, Tanaka et al. 2023). For the Stripe 82 and EGIS samples, we did not use this approach. Instead, we trained individuals using classifiers with many years of experience to identify features consistently. Although this method provides a more directed training process, it introduces potential visual bias and bias due to internal training. To mitigate these effects, all classifications were independently reviewed multiple times within our research group. Although some classifiers received guidance on how to identify specific features, the training was applied uniformly to maintain consistency. We acknowledge that using classifiers from the same group introduces an inherent risk of shared bias. Although complete elimination of subjectivity in visual classification is not possible, we have taken reasonable steps to reduce its influence and ensure the reliability of our results.

By using multiple survey images in conjunction with those from the SDSS to identify tidal structures, galaxies were cross-referenced to ensure that structures are not image artifacts or any other non-extragalactic structures. This has not been extensively done in other studies and can serve as a way to curb visual bias. For example, the HSC-SSP with its higher resolution images helped us identify 10 and 19 more galaxies with tidal features in the Stripe 82 and EGIS samples, respectively. Unfortunately, only 64% of the galaxies from Stripe 82 and 10.4% from EGIS are covered by the HSC-SSP. Based on the additional galaxies identified in HSC-SSP images and using the median Wald Normal Approximation value, if we had HSC-SSP data for all catalog galaxies, we could have found an additional $\sim 15 \pm 9$ and $\sim 177 \pm 81$ galaxies with tidal features, increasing our tidal fraction to about $7.6 \pm 1.1\%$ and $5.8 \pm 1.4\%$ for Stripe 82 and EGIS respectively. This shows that the possible reason for the difference in tidal fraction between Stripe 82 and EGIS is the amount that the HSC-SSP covers for each sample.

5.2 Projection Effects

Another factor that plays a role in visual classification bias is projection effects. The vast majority of studies on tidal features use samples of galaxies with varying inclination angles, including the studies discussed above. The varying inclination angles can hide or change the shape of tidal features, making it difficult to provide accurate classifications. Martin et al. (2022) found that for deep imaging, the uncertainty from projection was dominant for their images. In the case of our samples, only edge-on galaxies are used, which helps to eliminate most projection effects and keeps the tidal classifications consistent. Due to this, projection effects are not expected to play a significant role in our results.

5.3 Redshift Bias

As shown in Fig. 3.2, galaxies exhibiting tidal structures in the Stripe 82 sample tend to have lower spectroscopic redshifts, with a distribution peaking at $z \simeq 0.06$, and a mean of $z = 0.07$. For galaxies with tidal structures, the distribution peaks at $z \approx 0.04$. In the EGIS sample (Fig. 4.1), galaxies with tidal structures also tend to reside at lower redshifts, with both the peak and mean redshift at $z = 0.025$ and $z = 0.04$, respectively. To quantitatively assess whether galaxies with tidal structures are found at significantly lower redshifts than those without, we performed a Mann–Whitney U test. For the Stripe 82 sample, the resulting p-value of $p = 0.07$ suggests that the difference in redshift distributions is not statistically significant, although a slight shift toward lower redshifts for galaxies with tidal features is still evident. In contrast, the EGIS sample yields a p-value of $p = 0.03$, allowing us to reject the null hypothesis and conclude that galaxies with tidal structures are statistically more likely to be found at lower redshifts than those without. These results are consistent with both observational studies and simulations (Kado-Fong et al. 2018, Martin et al. 2022, Domínguez Sánchez et al. 2023), which find that the detection of tidal structures becomes increasingly difficult

at higher redshifts due to cosmological surface brightness dimming and reduced spatial resolution (Kado-Fong et al. 2018).

Analysing the redshifts from our samples using $(1+z)^3$ for AB magnitudes (see Whitney et al. 2020) to account for cosmological dimming, the average dimming value is found to be 1.2±0.15 and 1.14±0.07 for Stripe 82 and EGIS, respectively. This is not a significant enough change in the surface brightness; therefore, cosmological dimming should not play a significant role in our samples. Further evidence can be seen in Fig. 5.4, where the average offset between the surface brightness of the measured tidal features and their intrinsic surface brightness before cosmological dimming is ~ 0.09 and ~ 0.05 for Stripe 82 and EGIS, respectively, which are not significant offsets. Looking at cosmological dimming values greater than or equal to 1.5, it is found that three galaxies with substructures met these criteria. Specifically, two of the three have a tidal structure and a cosmological dimming of ~ 2.3 ($\Delta\mu = 0.36$ mag arcsec^{-2}) and ~ 2.8 (surface brightness not measured), while the other has a dimming of 1.5. Therefore, cosmological dimming does not play a significant role in detecting tidal structures for both samples of galaxies and does not explain the lack of tidal structures in galaxy images.

5.4 Mass Bias

It has been found that the classification of tidal structures is mass-biased (Atkinson et al. 2013, Kado-Fong et al. 2018, Bílek et al. 2020, Jackson et al. 2023). That is, more structures are found around larger mass galaxies. This is expected, as more massive galaxies tend to be more luminous, as will the structures produced by minor/major interactions with these larger mass galaxies, making them easier to identify. Additionally, the number of major mergers that occur is expected to scale with the stellar mass of a galaxy, which means the number of substructures also scales with galaxy mass (Guzmán-Ortega et al. 2023). Bílek et al. (2020) found that galaxies with stellar masses

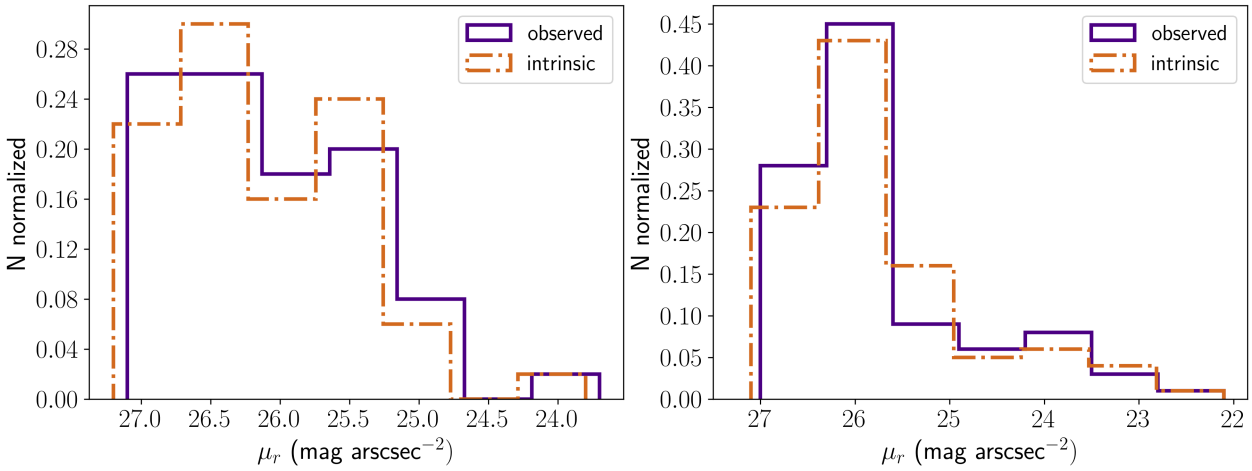

Figure 5.4 The distribution of the measured median surface brightness for all (left) and the "Best" (right) tidal structures in the *r* band for the Stripe 82 and EGIS samples, respectively. Each distribution is overlaid with another distribution of the intrinsic surface brightness calculated using the cosmological dimming values for each galaxy. A small offset can be seen for each image.

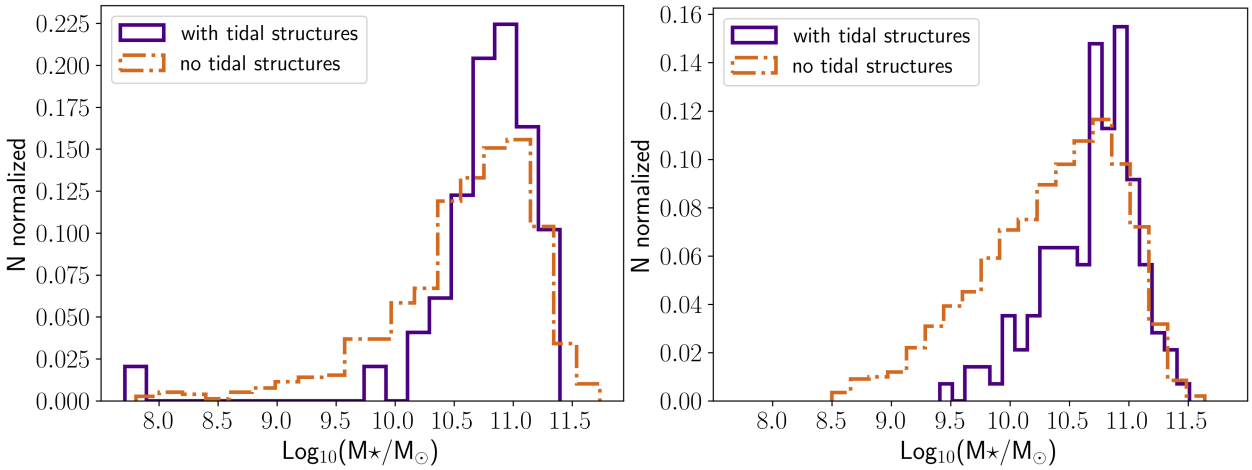

Figure 5.5 Stellar mass distribution for the Stripe 82 sample (left) and the EGIS sample (right). Both compare the masses of galaxies with tidal features and the rest of the sample. Mass was calculated using the $g-r$ color and the absolute magnitude in the *r* band.

above $10^{11}\,M_{\odot}$ had 1.7 times more tidal structures than those below this value. In a similar analysis, Jackson et al. (2023) found 1.2 times more tidal structures.

We used the following equation to compute the stellar mass of galaxies in both of our samples:

$$\log_{10}\left(\frac{M}{L}\right) = a_{\lambda} + (b_{\lambda} \times \text{color}) \tag{5.1}$$

The a_{λ} and the b_{λ} are -0.306 and 1.097, respectively, for the r band and for the $g-r$ color (Bell et al. 2003). It is important to note that the mass values calculated for both samples do not account for internal dust attenuation, but they are accurate enough for our general purposes.

To get a more accurate picture of the mass distribution and account for dust for the EGIS sample, we used 2MASS (Two Micron All Sky Survey; (Skrutskie et al. 2006)) magnitude data, which only accounts for 3,820 galaxies in the EGIS sample. We corrected the magnitudes and calculated the absolute magnitude using the following from Mosenkov et al. (2010)

$$M_{\lambda} = m_{\lambda} - A_{\lambda} - 25 - 5\log_{10}(D_L) \tag{5.2}$$

where m_{λ} is the apparent magnitude in each band, D_L is the luminosity distance, and A_{λ} is the Galactic extinction (Schlegel et al. 1998). The magnitudes were converted to the $B-V$ color using the following equation from Bilir et al. (2008)

$$(B-V)_0 = \alpha_1 (J-H)_0 + \beta_1 (H-K_s)_0 - \gamma_1 \tag{5.3}$$

where $\alpha_1 = 1.622$, $\beta_1 = 0.912$, and $\gamma_1 = 0.044$. This allowed us to use it with Eq. 5.1, setting a_{λ} and the b_{λ} to -0.261 and 0.433, respectively, using the absolute magnitudes in the J band to calculate the masses.

For stellar masses estimated using optical data, both of our samples suggest that the galaxies with more than one tidal feature have, on average, a stellar mass of $10^{10.6}\,M_{\odot}$ and $10^{10.7}\,M_{\odot}$ for Stripe 82 and EGIS, respectively. In Fig. 5.5, galaxies with structures peak at $\sim 10^{11}\,M_{\odot}$ for both samples, in

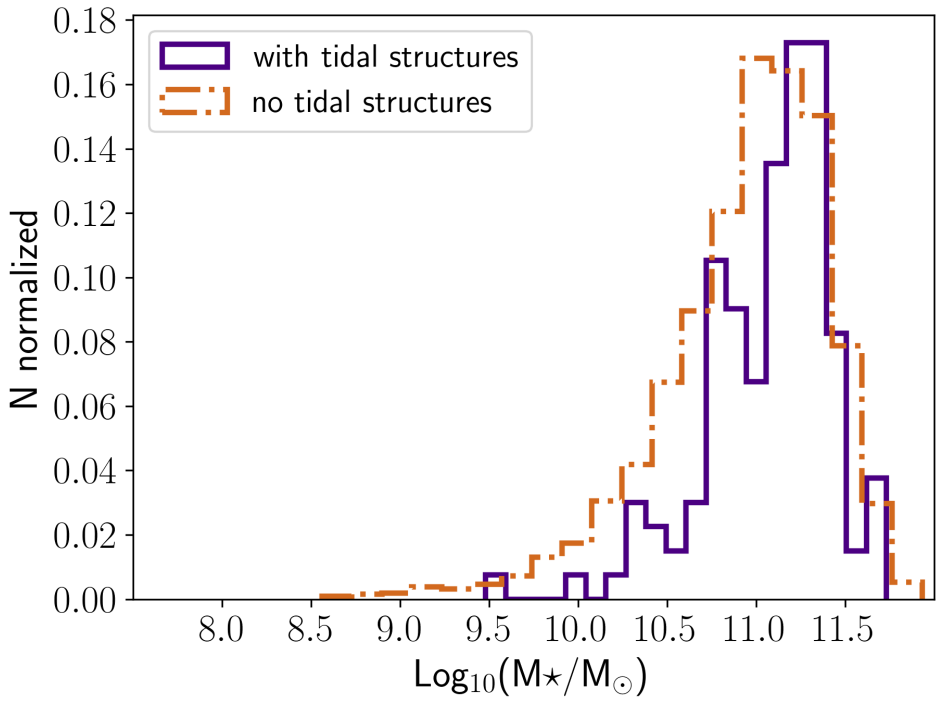

Figure 5.6 The mass distribution for the EGIS sample using 2MASS magnitudes for galaxies with tidal features and the rest of the sample. Mass was calculated using the $B-V$ color and the absolute magnitude in the J band.

agreement with Jackson et al. (2023). We performed a Mann-Whitney test of the null hypothesis that the distribution underlying the sample of galaxy masses with tidal structures is the same as the distribution underlying the sample of galaxy masses without tidal structures for both samples. The p-values obtained from these two samples are $p = 0.04$ and $p = 7.8 \times 10^{-13}$. Therefore, we can reject the null hypothesis and conclude that the two sub-samples from both samples are not similar.

Likewise, the results for stellar masses estimated using 2MASS observations are shown in Fig. 5.6, where the masses appear slightly larger because the 2MASS J, H, and K bands penetrate dust more effectively within the galaxies. Galaxies with tidal structures peak at $\sim 10^{11.3}\,M_{\odot}$ and the two distributions have a $p = 7.5 \times 10^{-4}$. Therefore, as indicated by both Figs. 5.5 and 5.6, we confirm a correlation between stellar mass and the presence of tidal structures in our sample galaxies.

5.5 Surface Brightness of Features

Another possible reason for the lack of tidal structures in the current study could be that our data is not yet deep enough to detect the faintest LSB features. Johnston et al. (2008) shows that the majority of tidal structures are expected to have a peak surface brightness fainter than ~ 30 mag arcsec^{-2}. However, Sola et al. (2022) found that the tidal features in their sample did not extend beyond the depth of a median value of 27.5 mag arcsec^{-2}. We conducted a similar investigation of the depth of the tidal structures within both ES82 and EGIS samples. For Stripe 82, polygon regions were created around the structures themselves using SAO DS9. As for the EGIS sample, due to the time-consuming nature of constructing regions around features by hand and the large sample size, a different approach was taken. A novel GUI, similar to the GUI constructed for lopsided and warped galaxies, was created to speed up the processes of measuring the LSB tidal features. This GUI allows the user to use the isophotes and a selected area to create regions that accurately encompass tidal features, as seen in Fig. 5.7. Unlike Stripe 82, only the "Best" tidal structures in the EGIS sample were measured.

From our measurements, we were able to find that both our samples of tidal structures do not extend beyond the photometric depth of a median value of ~ 27.1 mag arcsec^{-2} in the r-deep and r band (see Fig. 5.4). This result is similar to that of Sola et al. (2022) and could indicate that these structures have not had enough time to accrete onto their host galaxy and dissipate, therefore remaining luminous. The mass of the host galaxies may also contribute, as all galaxies with tidal features in our samples are massive and therefore more luminous, which likely enhances the visibility of their associated tidal structures. This could also mean that neither of our samples is deep enough, as only the more luminous structures are discernible, whereas the deeper structures are overlooked and missed completely. As shown in Fig. 5.4, the measured surface brightness of the tidal structures for both samples peaks at 26.5 mag arcsec^{-2} and the Stripe 82 sample has an average

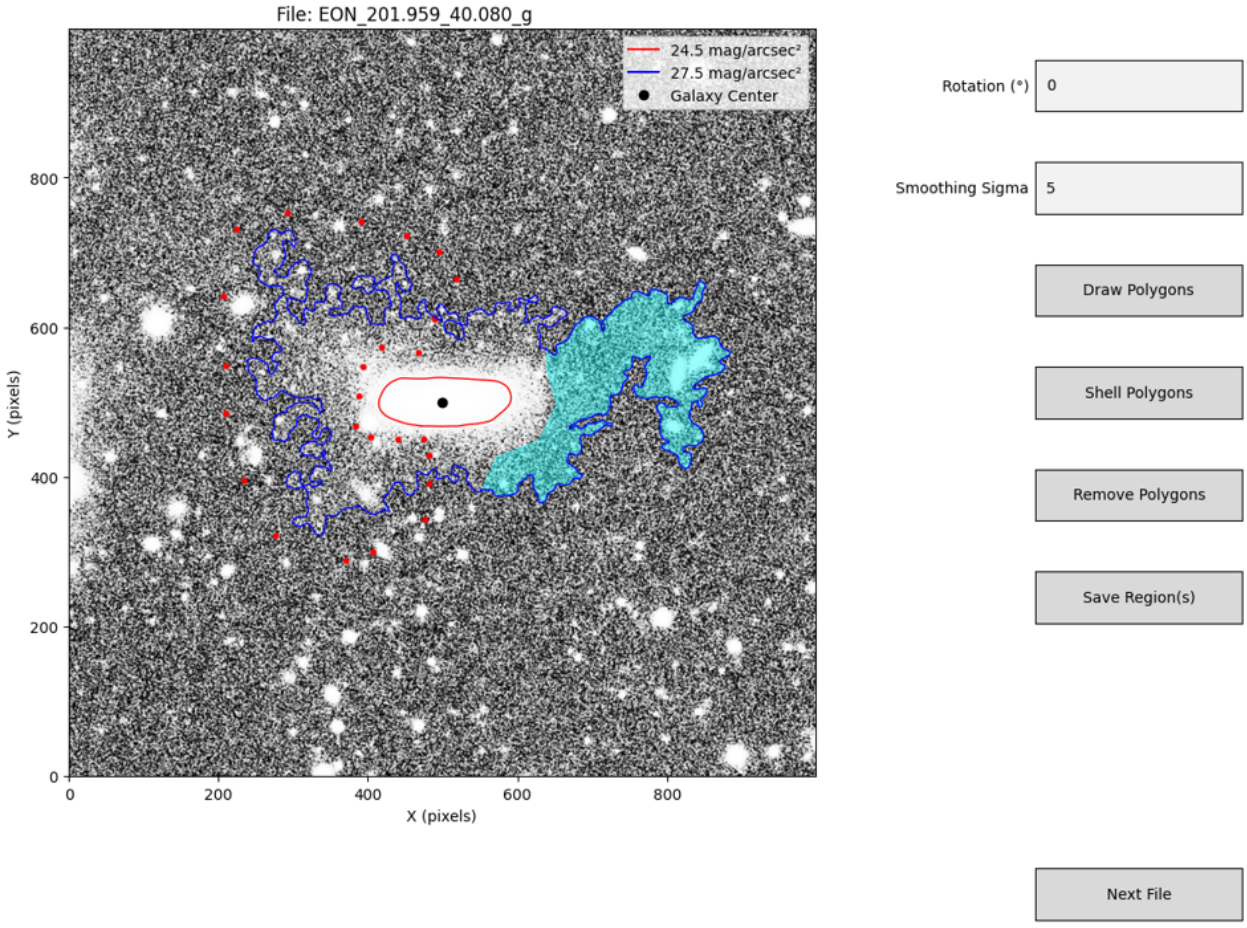

Figure 5.7 An example of the Surface Brightness GUI that gives the user different options to accurately measure tidal features. The red dots represent where the user has clicked to select the part of the isophote they want measured. The filled-in cyan area represents a previously selected feature that the user wants measured. Multiple features can be selected for measurement. The example galaxy exhibits a tidal stream and some plumes.

of 26.1 ± 0.7 mag arcsec^{-2}, while the EGIS sample has an average of 25.8 ± 0.7 mag arcsec^{-2}. In Sola et al. (2022), their average is 25.6 ± 0.7 mag arcsec^{-2}, which matches our measurements.

5.6 Summary

In summary, both of our catalogs of edge-on galaxies predominantly include high-mass, low-redshift systems observed with sufficiently deep imaging that accounts for Galactic cirrus. Cosmological

simulations indicate that these parameters provide the best opportunity to identify a large fraction of tidal structures. Therefore, the relatively low detection rates in our samples (compared to some observational studies and simulations) may result from a combination of visual biases and insufficient image depth to reveal features around higher-redshift galaxies in both samples. Additionally, discrepancies may arise because other observational studies often have smaller, incomplete samples and do not adequately account for Galactic cirrus contamination.

Another reason not mentioned earlier could be that the predicted fraction of tidal structures that should be observed in cosmological simulations could be inaccurate. Although cosmological simulations have had great success in producing observed characteristics of galaxies such as hierarchical structure formation and reproducing the general properties of galaxies (Somerville & Davé 2015, Ward et al. 2022, Baes et al. 2024) they are not infallible and can produce discrepancies between prediction and observation. For example, the long-standing discrepancy of the star formation rate vs. stellar mass relation gives a steeper slope than observed for lower mass galaxies at intermediate redshifts (Daddi et al. 2007, Christensen et al. 2012, Somerville & Davé 2015). More recent discrepancies have been found, such as the disparities in metallicity recycling and mixing history for larger galaxies (Jara-Ferreira et al. 2024). Such discrepancies possibly arise from not having a clear understanding of the mechanisms that govern specific physical processes such as star formation and stellar feedback (Somerville & Davé 2015). This lack of understanding could explain why the few studies discussed above and our own do not match cosmological simulations. As noted above, Miro-Carretero et al. (2024) reported lower predicted tidal fractions that more closely align with our results, particularly when using the TNG50 and Auriga simulations. Their findings suggest that the specific framework a simulation uses can significantly influence the predicted visibility of tidal features. Thus, the type of simulation employed may be a key factor in understanding the disparity between theoretical expectations and observational data.

Additionally, simulations such as the one used in Martin et al. (2022) produce 'smooth' images or images that do not contain contaminants, background/foreground objects (stars and galaxies), sky subtraction residuals, imaging artifacts, etc. (Domínguez Sánchez et al. 2023). This allows the classifiers to know that the structures seen in the mock images are true structures, leading to higher fraction counts. Another point to consider is the morphology of the galaxies being produced in simulations. Disk galaxies or late-type galaxies (LTGs) have been found to be more easily disrupted and will produce tidal features more easily than compact spheroids (Kormendy et al. 2009, Pedrosa et al. 2014). If a simulation produces more disk galaxies than spheroidal galaxies, then it is possible that the simulation would produce a higher fraction of tidal features. Looking specifically at the IllustrisTNG (Marinacci et al. 2018, Naiman et al. 2018, Nelson et al. 2018, Pillepich et al. 2018, Springel et al. 2018, Nelson et al. 2019) and EAGLE simulations (Crain et al. 2015, Schaye et al. 2015), the morphology of the simulated galaxies matched observations, where only the asymmetry is larger for the simulated galaxies (Bignone et al. 2020, Guzmán-Ortega et al. 2023). The NEWHORIZON simulation used by Martin et al. (2022) also agrees well with the observed morphology (Dubois et al. 2021). This means that the morphology in simulations does not account for the observed discrepancy in LSB features.

This discussion prompted us to look at the morphology of the galaxies in our samples using the HyperLeda database. For the entire Stripe 82 sample, 519 (62%) are LTGs, 295 (35.2%) are early-type galaxies (ETGs), and 24 (2.9%) have an unknown morphology. Looking at only tidal structures, 32 galaxies (65.3%) are LTGs, and 17 (21.1%) are ETGs. Eleven of the LTGs had uncertain classifications and were further classified by eye. Of the three galaxies that contain more than one tidal structure, two are ETGs and one is an LTG. For the EGIS sample, we find that 5,727 (99.7%) are LTGs while 18 are unknown. It is known that more tidal features are found around ETGs due to their formation and evolution mechanism being minor and major mergers, which produce more easily visible features such as plumes (Duc 2017) and shells (Yoon & Lim 2020). With the

majority or entirety of our samples consisting of LTGs, another reason for the discrepancy could be that our sample lacks enough ETGs. Many of the studies mentioned focus either solely on ETGs or have a more balanced split between ETGs and LTGs. Additionally, these studies often have varying surface brightness limits. Both effects may lead to different tidal feature fractions.

It is difficult to pinpoint the exact cause of the discrepancy in LSB frequency between simulations and observations, but our discussion above suggests it likely arises from a combination of factors — primarily that our samples lack sufficient depth, are dominated by LTGs, and that there may be some inaccuracies within the simulations. Deep photometric studies of large, complete samples of galaxies, such as the LSST, should better describe the statistics of tidal structures in the local Universe for a more appropriate comparison with cosmological simulations.

Chapter 6

Conclusion

In this thesis, we have presented two statistically complete, large samples of edge-on galaxies from Stripe 82 (838 galaxies) and EGIS (5,745 galaxies). We have compiled two catalogs and produced the largest atlas of low surface brightness features around edge-on galaxies to date. Each sample incorporates data from three sky surveys — SDSS, DESI Legacy Imaging Surveys, and HSC-SSP. Additionally, we obtained observations of 16 EGIS galaxies using the ARCTIC instrument on the APO 3.5m telescope. These combined datasets enabled the classification of LSB tidal and other distinctive structures, improving classification accuracy. To aid in analysis, two graphical user interfaces were developed for measuring warped and lopsided galaxies, as well as the surface brightness of tidal features. The conclusions of this study can be summarized as follows:

1. We compiled a new catalog of 838 edge-on galaxies located in the SDSS Stripe 82 region. Key properties of these galaxies were derived, including a mean spectroscopic redshift of $\langle z_{\rm spec} \rangle = 0.06^{+0.03}_{-0.02}$, as shown in Fig. 3.2. The sample also has an average absolute magnitude in the r-band of $\langle M_r \rangle = -20.7^{+0.8}_{-0.7}$ (Fig. 3.3), which aligns well with the values reported by Bizyaev et al. (2014) for galaxies in the EGIS catalog.

2. We compiled a new catalog using the 5,745 edge-on galaxies from the online EGIS catalog presented in Bizyaev et al. (2014). By collecting data from different sources and processing galaxy images to enhance features, we have created the largest atlas of features around edge-on galaxies. Key properties are derived, such as stellar mass and redshifts. The mean spectroscopic redshift of the sample is $\langle z_{\rm spec} \rangle = 0.04^{+0.06}_{-0.03}$.

3. The classification of galaxies by the presence of structures has been performed. The availability of imaging from three independent surveys was crucial to this process, as their combined depth and improved angular resolution significantly enhanced our ability to identify and confirm these features. Additionally, the application of a new image processing technique for the EGIS galaxies, alongside the multi-survey approach, increases confidence that the detected features represent genuine galactic structures rather than imaging artifacts.

4. For the Stripe 82 sample, there are 49 (5.8%) galaxies with LSB tidal structures (tails, bridges, arcs, shells, satellite remnants, disk deformations) and 56 (6.7%) galaxies with distinctive structural features (thin disk warps, lopsided disks, and polar structures).

5. For the EGIS sample, there are 159 (2.8%) and 236 (4.1%) galaxies with tidal structures (for the highest confidence and all confidences, respectively. An automatic method for measuring and detecting galaxy warps and lopsidedness was developed in conjunction with a GUI. We find 2,458 (42.8%) galaxies with warps and 1,965 (34.2%) galaxies with lopsidedness, in good agreement with observational studies. In contrast to previous studies, our sample exhibits a smaller fraction of S-type warps.

6. A key finding of this thesis is that, despite the depth of the images analyzed, the fraction of galaxies exhibiting LSB tidal structures in both the Stripe 82 and EGIS samples is considerably lower than reported in other studies based on modern cosmological simulations of galaxy formation. This discrepancy likely results from a combination of factors, including the limited

depth of our samples, their predominance of late-type galaxies, and potential inaccuracies within the simulations. Additionally, we conclude that Galactic cirrus and cosmological surface brightness dimming do not significantly affect the structural statistics in our analysis.

Based on the results and discussion of this thesis, the agreement between the large samples of Stripe 82, EGIS, and the work of Kado-Fong et al. (2018), suggests that the rarity of observable tidal features may be a genuine reflection of their occurrence rather than a limitation of our samples. While factors such as visual bias, the morphological composition of the samples (notably the high fraction of late-type galaxies), and imaging depth can influence classification to some extent, their impact may only be secondary. In particular, imaging depth, though often cited as a limiting factor, cannot fully account for the discrepancy, especially in light of cosmological simulations that generate mock observations at varying depths. These simulations predict a higher incidence of tidal features at comparable surface brightness limits, yet our observed counts remain consistently lower. This indicates that the root of the discrepancy likely lies not in the observational data but in the simulations themselves and possibly in the type of simulation. It is therefore crucial to examine whether current cosmological models accurately represent the physical processes driving galaxy interactions, such as tidal stripping, merger histories, and stellar feedback.

Chapter 7

Appendix

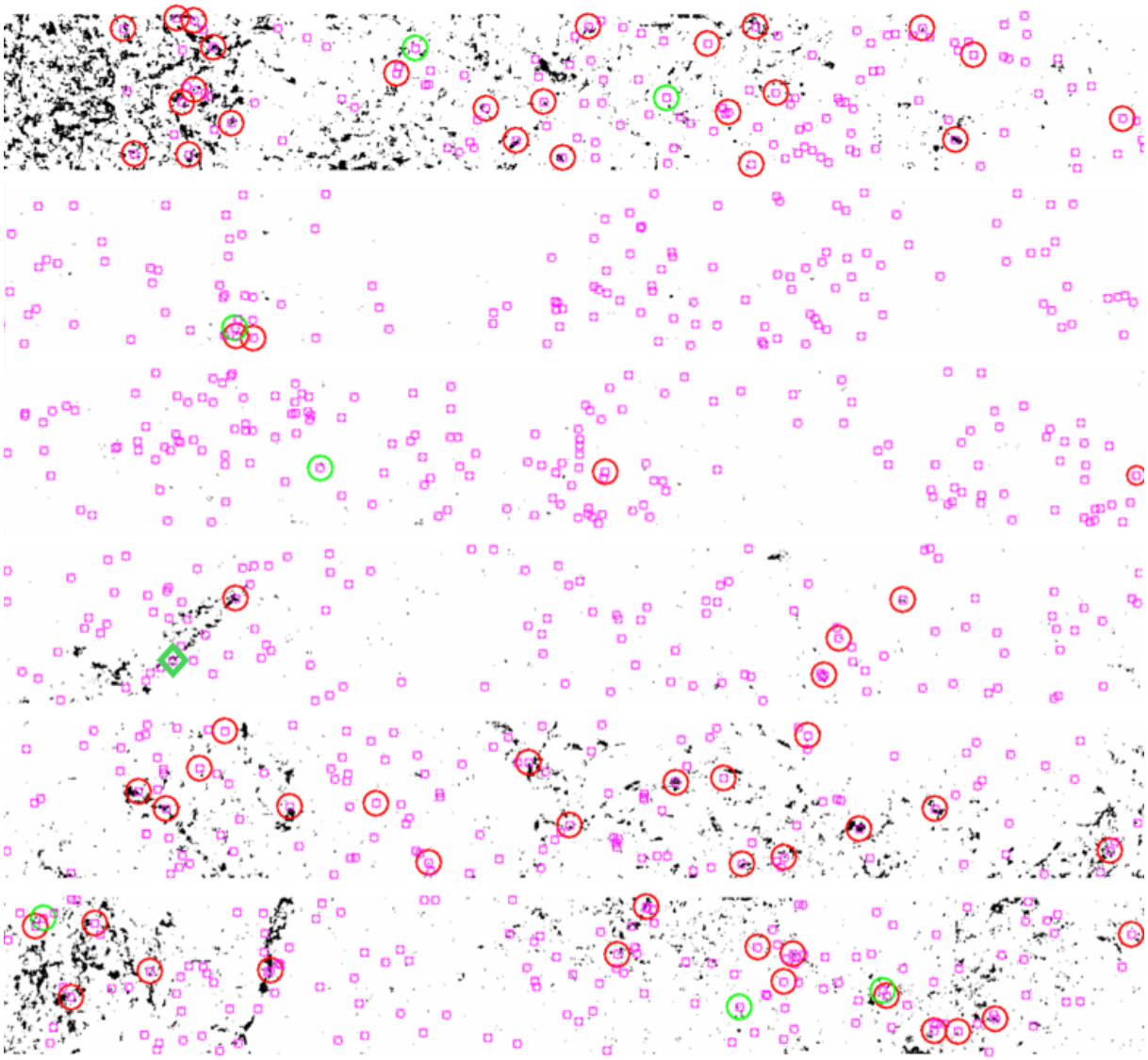

Figure 7.1 A series of six stacked strips showing the Milky Way's cirrus clouds where the purple boxed circles show where each galaxy within our catalog is located. Each strip, going from left to right, covers approximately 18 degrees of the sky. This covers a total of 110 degrees in R.A. The R.A. ranges from 60° to 0° which includes the first three strips and then 360° to 310° which includes the last three strips. The Dec. ranges from -1.25° to 1.25°. These images are constructed from a single image (available on https://physics.byu.edu/faculty/mosenkov/docs/cirrus_wcs.fits) that spans the entire SDSS Stripe 82 (Smirnov et al. 2023). 64 (red circles) out of 838 galaxies fall within or near a cirrus cloud. The seven green circles represent the galaxies that have tidal features. The one green diamond represents the galaxy that was removed as a tidal feature candidate.

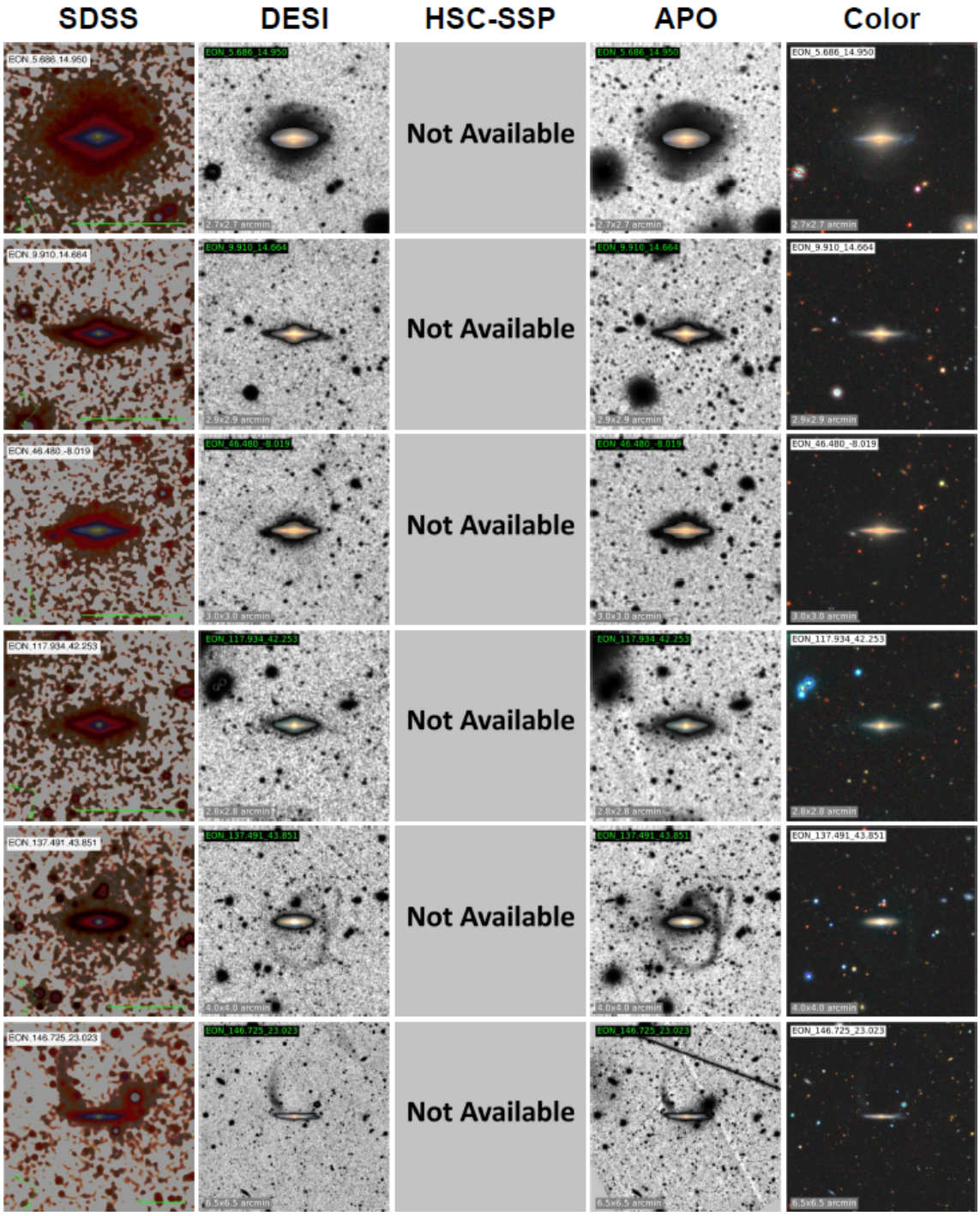

Figure 7.2 The first set of APO images are presented with three independent surveys: the first column is SDSS co-adds and (created using g, r, and i bands), the second, third, and fourth columns are images from DESI Legacy, HSC-SSP (co-adds), and APO, respectively, while the fifth column is is RGB of DESI (created using g, r, and z bands).

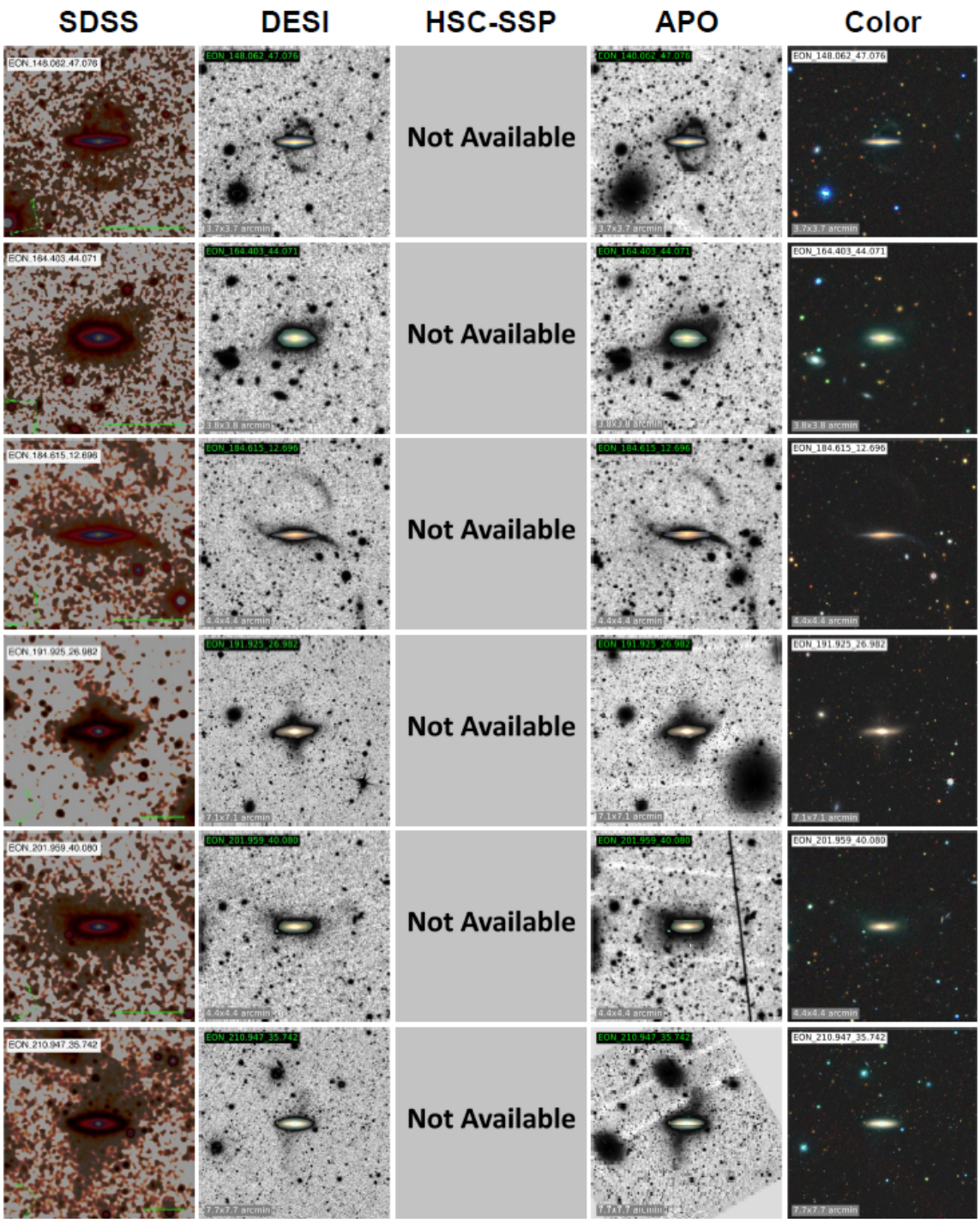

Figure 7.3 The second set of APO images are presented with three independent surveys: the first column is SDSS co-adds and (created using g, r, and i bands), the second, third, and fourth columns are images from DESI Legacy, HSC-SSP (co-adds), and APO, respectively, while the fifth column is is RGB of DESI (created using g, r, and z bands).

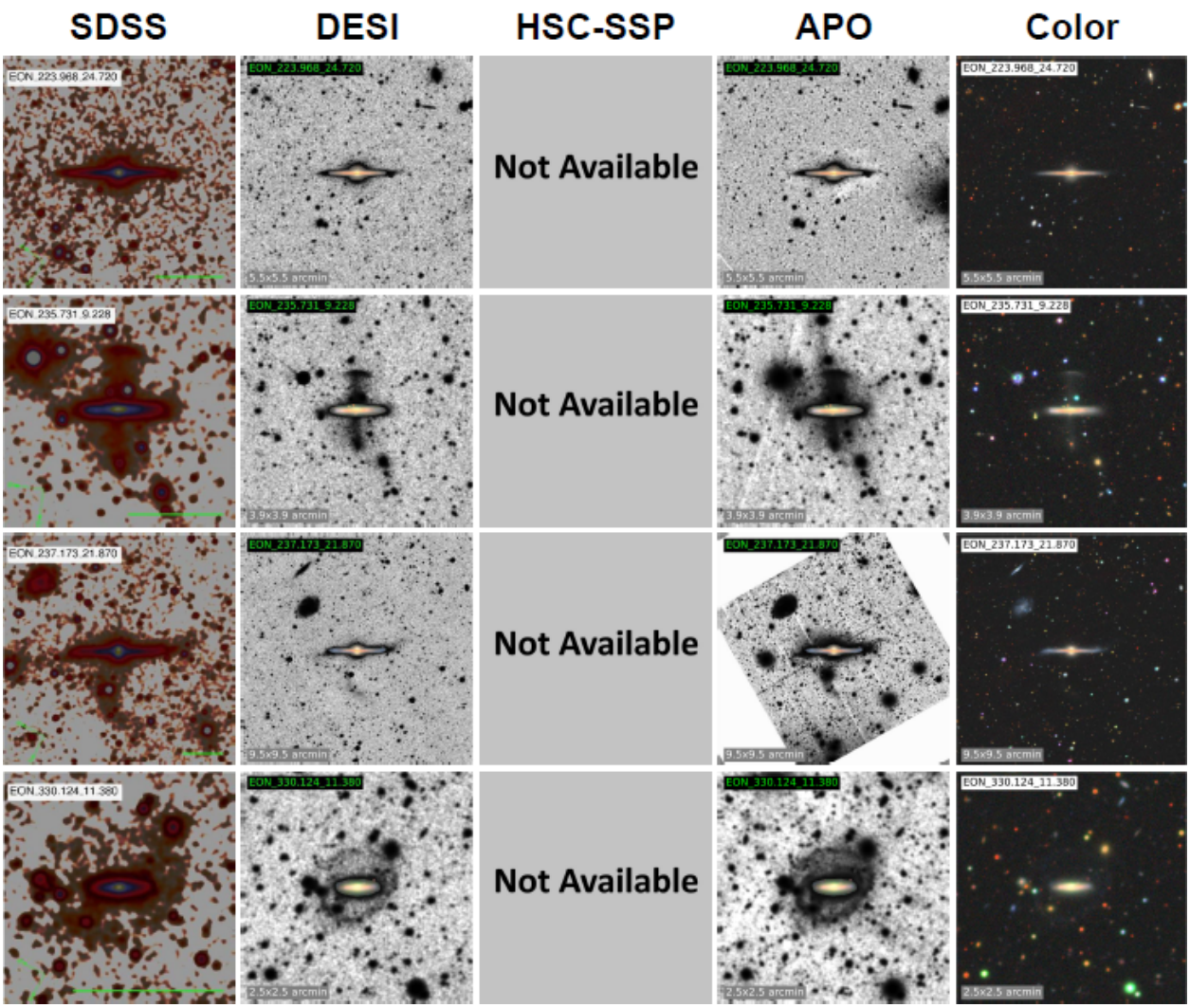

Figure 7.4 The third set of APO images are presented with three independent surveys: the first column is SDSS co-adds and (created using g, r, and i bands), the second, third, and fourth columns are images from DESI Legacy, HSC-SSP (co-adds), and APO, respectively, while the fifth column is is RGB of DESI (created using g, r, and z bands).

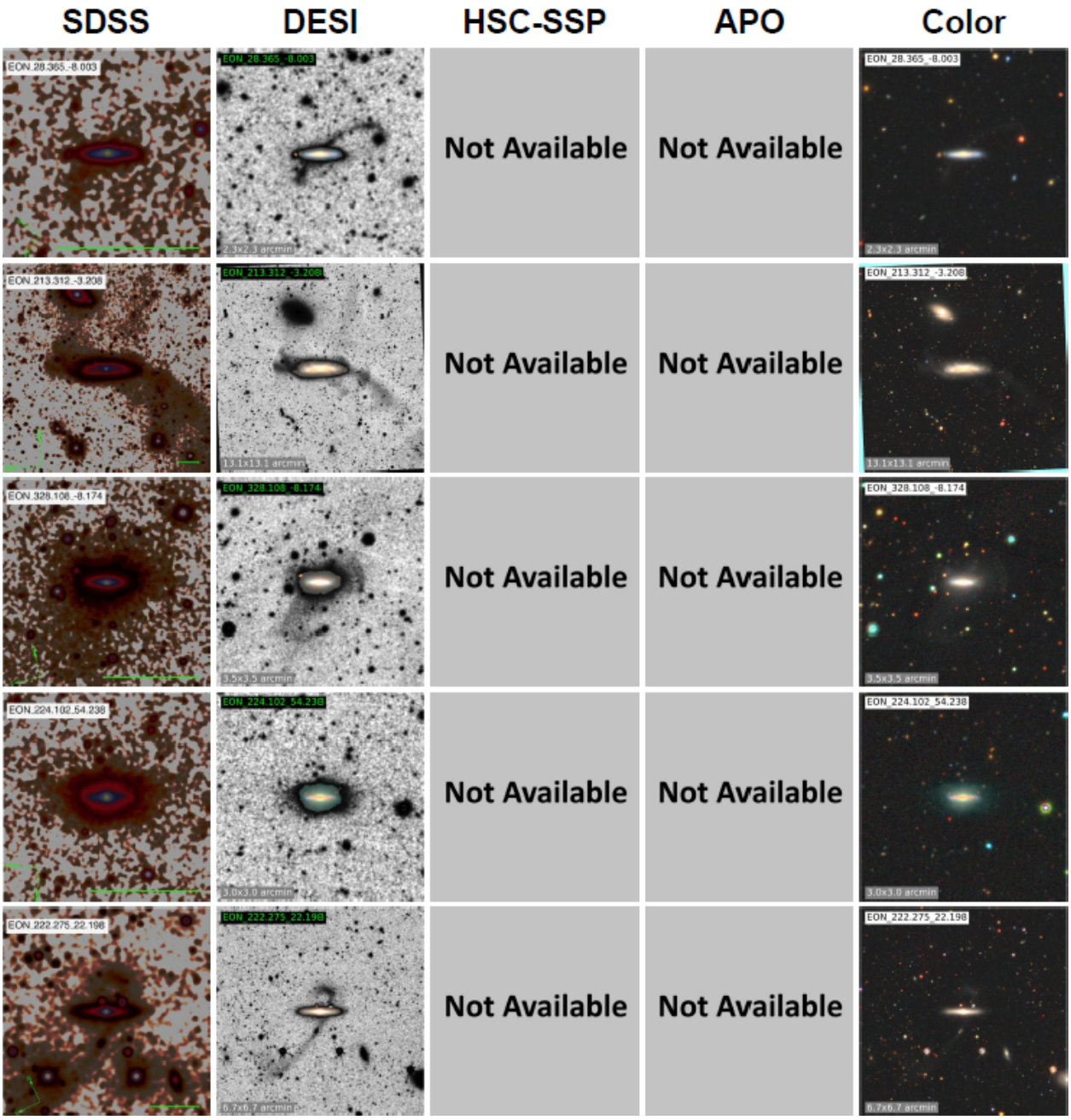

Figure 7.5 Examples of observed tidal structures are demonstrated in three independent surveys and supplementary observations using APO: the first column is SDSS co-adds and (created using g, r, and i bands), the second, third, and fourth columns are images from DESI Legacy, HSC-SSP (co-adds), and APO, respectively, while the fifth column is is RGB of DESI (created using g, r, and z bands). Each line demonstrates a galaxy with a stellar stream, a tidal tail, a shell and plume, an asymmetric halo, and a bridge, respectively.

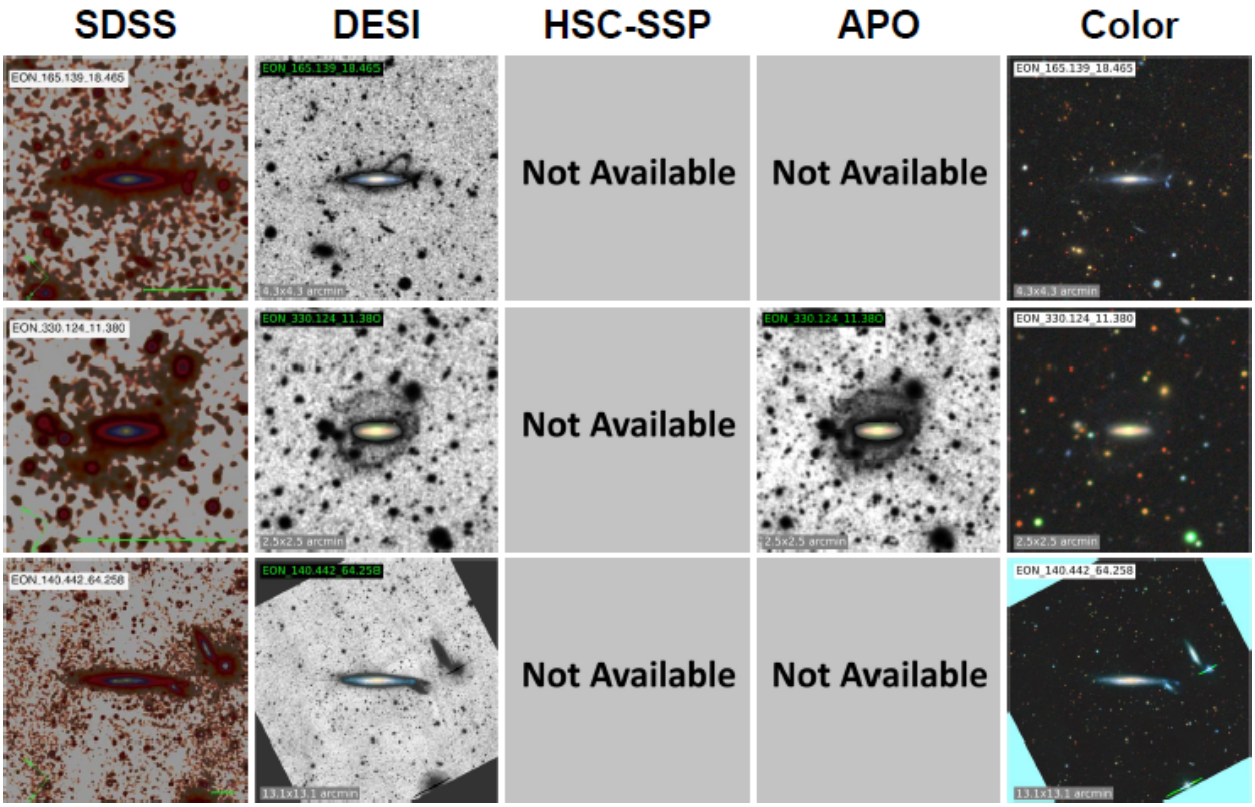

Figure 7.6 A continuation of examples of observed tidal structures as presented in Fig. 7.5. Each line demonstrates a galaxy with an arc, a loop, and satellite debris, respectively.

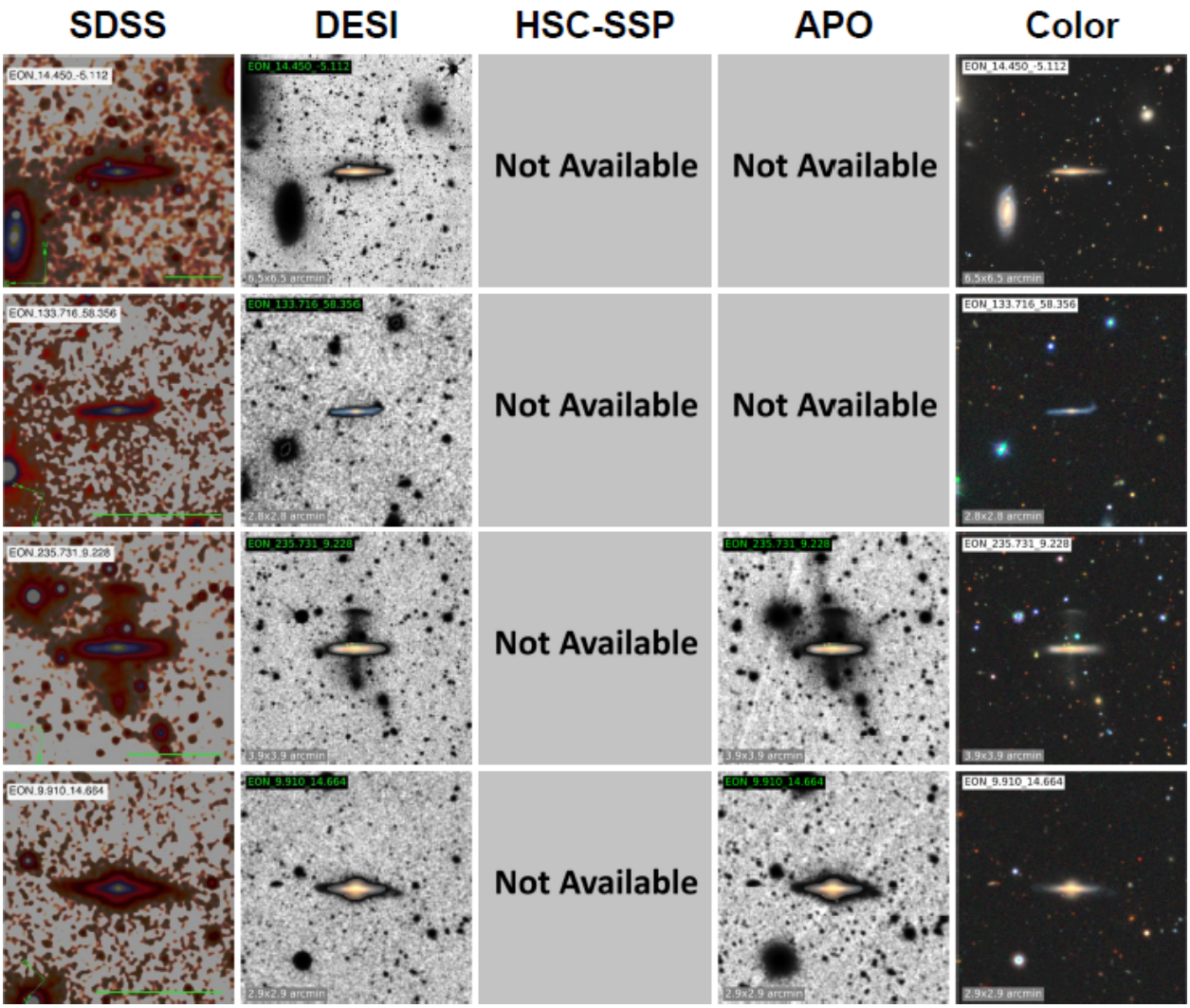

Figure 7.7 Examples of observed tidal structures are demonstrated in three independent surveys and supplementary observations using APO: the first column is SDSS co-adds and (created using g, r, and i bands), the second, third, and fourth columns are images from DESI Legacy, HSC-SSP (co-adds), and APO, respectively, while the fifth column is is RGB of DESI (created using g, r, and z bands). Each line demonstrates a galaxy with a lopsided disk, a warp, a polar ring, and a polar bulge, respectively.

EON_137.491_43.851

SDSS

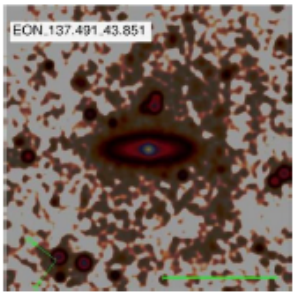

DESI

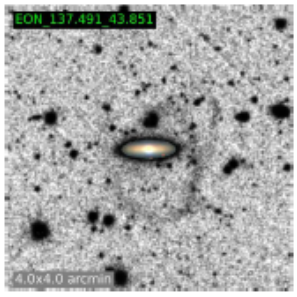

HSC-SSP

Not Available

APO

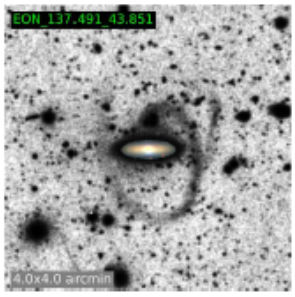

DESI Color

Identifiers				
EGIS Name	Cross-Identifications			
EON_137.491_43.851	WISEA J090957.90+435104.1; 2MASX J09095786+4351045; 2MASXi J0909578+435104; 2MASS J09095790+4351042; SDSS J090957.89+435103.9			
Position Coordinates(Equatorial J2000) and Redshift				
RA, DEC	RA, DEC (Deg)	Redshift	Redshift Flag	
9h9m57.9s, +43d51m4s	137.491257, 43.851112	0.02598	SLS	
Tidal Classifications				
Streams/Tails	Shells/Plumes	Bridges	Arcs and Loops	Satellite Debris
Yes	N/A	N/A	N/A	N/A
Structure Classifications				
Polar Structure	Lopsided	Tilted Outer Structure	Warps	
N/A	N/A	N/A	N/A	
Edge-on Morphology		Galactic Cirrus		
Almost Edge-on		N/A		
Notes				
N/A				

1306

Figure 7.8 A page taken from the official Atlas.

Bibliography

Abazajian, K. N., et al. 2009, ApJS, 182, 543

Abraham, R. G., & van Dokkum, P. G. 2014, PASP, 126, 55

Ahumada, R., et al. 2020, ApJS, 249, 3

Aihara, H., et al. 2022, PASJ, 74, 247

Ann, H. B., & Bae, H. J. 2016, Journal of Korean Astronomical Society, 49, 239

Ann, H. B., & Park, J. C. 2006, New A, 11, 293

Annis, J., et al. 2014, ApJ, 794, 120

Atkinson, A. M., Abraham, R. G., & Ferguson, A. M. N. 2013, ApJ, 765, 28

Baes, M., et al. 2024, A&A, 683, A182

Bahr, S. K. H., & Mosenkov, A. V. 2025, arXiv e-prints, arXiv:2505.13653

Baillard, A., et al. 2011, A&A, 532, A74

Baldwin, J. E., Lynden-Bell, D., & Sancisi, R. 1980, MNRAS, 193, 313

Barnes, J. E. 1992, ApJ, 393, 484

Barrabés, E., Cors, J. M., Garcia-Taberner, L., & Ollé, M. 2017, MNRAS, 472, 2554

Bekki, K. 1997, ApJ, 490, L37

—. 1998, ApJ, 499, 635

Bell, E. F., McIntosh, D. H., Katz, N., & Weinberg, M. D. 2003, ApJS, 149, 289

Belokurov, V., et al. 2006, ApJ, 642, L137

Bertin, E., & Arnouts, S. 1996, A&AS, 117, 393

Bignone, L. A., Pedrosa, S. E., Trayford, J. W., Tissera, P. B., & Pellizza, L. J. 2020, MNRAS, 491, 3624

Bílek, M., et al. 2020, MNRAS, 498, 2138

Bilir, S., Ak, S., Karaali, S., Cabrera-Lavers, A., Chonis, T. S., & Gaskell, C. M. 2008, MNRAS, 384, 1178

Bizyaev, D. V., Kautsch, S. J., Mosenkov, A. V., Reshetnikov, V. P., Sotnikova, N. Y., Yablokova, N. V., & Hillyer, R. W. 2014, ApJ, 787, 24

Blumenthal, K. A., et al. 2020, MNRAS, 492, 2075

Bottrell, C., Simard, L., Mendel, J. T., & Ellison, S. L. 2019, MNRAS, 486, 390

Bournaud, F., & Combes, F. 2003, A&A, 401, 817

Bournaud, F., Combes, F., Jog, C. J., & Puerari, I. 2005, A&A, 438, 507

Boylan-Kolchin, M., Ma, C.-P., & Quataert, E. 2008, MNRAS, 383, 93

Bridge, C. R., Carlberg, R. G., & Sullivan, M. 2010, ApJ, 709, 1067

Brook, C. B., Governato, F., Quinn, T., Wadsley, J., Brooks, A. M., Willman, B., Stilp, A., & Jonsson, P. 2008, ApJ, 689, 678

Brough, S., et al. 2020, arXiv e-prints, arXiv:2001.11067

Byrd, G. G., & Howard, S. 1992, AJ, 103, 1089

Christensen, C., Quinn, T., Governato, F., Stilp, A., Shen, S., & Wadsley, J. 2012, MNRAS, 425, 3058

Cooper, A. P., D'Souza, R., Kauffmann, G., Wang, J., Boylan-Kolchin, M., Guo, Q., Frenk, C. S., & White, S. D. M. 2013, MNRAS, 434, 3348

Cooper, A. P., et al. 2011, ApJ, 743, L21

Crain, R. A., et al. 2015, MNRAS, 450, 1937

Daddi, E., et al. 2007, ApJ, 670, 156

Dalcanton, J. J., & Bernstein, R. A. 2002, AJ, 124, 1328

de Grijs, R. 1998, MNRAS, 299, 595

de Vaucouleurs, G., de Vaucouleurs, A., Corwin, Herold G., J., Buta, R. J., Paturel, G., & Fouque, P. 1991, Third Reference Catalogue of Bright Galaxies (Springer, New York, NY (USA))

Dekel, A., et al. 2009, Nature, 457, 451

Dey, A., Schlegel, D. J., & Lang. 2019, AJ, 157, 168

Dolfi, A., Gómez, F. A., Monachesi, A., Varela-Lavin, S., Tissera, P. B., Sifón, C., & Galaz, G. 2023, MNRAS, 526, 567

Domínguez Sánchez, H., et al. 2023, MNRAS, 521, 3861

Dubois, Y., et al. 2021, A&A, 651, A109

Duc, P.-A. 2017, in Formation and Evolution of Galaxy Outskirts, ed. A. Gil de Paz, J. H. Knapen, & J. C. Lee, Vol. 321, 180–182

Duc, P. A., Cuillandre, J. C., Karabal, E., Cappellari, M., Alatalo, K., Blitz, L., & Bournaud, F. 2014, MNRAS, 446, 120

Duc, P.-A., & Renaud, F. 2013, in Lecture Notes in Physics, Berlin Springer Verlag, ed. J. Souchay, S. Mathis, & T. Tokieda, Vol. 861 (Springer-Verlag Berlin Heidelberg), 327

Duc, P.-A., et al. 2015, MNRAS, 446, 120

Ebrova, I. 2013, Phd thesis, Charles University in Prague, arXiv:1312.1643

Fliri, J., & Trujillo, I. 2016, MNRAS, 456, 1359

Font, A. S., et al. 2011, MNRAS, 417, 1260

Frenk, C. S., & White, S. D. M. 2012, Annalen der Physik, 524, 507

Fry, A. M., Morrison, H. L., Harding, P., & Boroson, T. A. 1999, AJ, 118, 1209

García de la Cruz, J., Martig, M., & Minchev, I. 2023, MNRAS, 518, 5403

Gilhuly, C., et al. 2020, ApJ, 897, 108

—. 2022, ApJ, 932, 44

Giovanelli, R., Haynes, M. P., Salzer, J. J., Wegner, G., da Costa, L. N., & Freudling, W. 1994, AJ, 107, 2036

Gómez, F. A., White, S. D. M., Grand, R. J. J., Marinacci, F., Springel, V., & Pakmor, R. 2017, MNRAS, 465, 3446

Guzmán-Ortega, A., Rodriguez-Gomez, V., Snyder, G. F., Chamberlain, K., & Hernquist, L. 2023, MNRAS, 519, 4920

Hart, R. E., et al. 2016, MNRAS, 461, 3663

Hubble, E. P. 1926, ApJ, 64, 321

Ienaka, N., Kawara, K., Matsuoka, Y., Sameshima, H., Oyabu, S., Tsujimoto, T., & Peterson, B. A. 2013, ApJ, 767, 80

Illingworth, G. D., et al. 2013, ApJS, 209, 6

Ivezić, Ž., et al. 2019, ApJ, 873, 111

Jackson, T. M., Pasquali, A., La Barbera, F., More, S., & Grebel, E. K. 2023, MNRAS, 520, 1155

Jara-Ferreira, F., Tissera, P. B., Sillero, E., Rosas-Guevara, Y., Pedrosa, S. E., De Rossi, M. E., Theuns, T., & Bignone, L. 2024, MNRAS, 530, 1369

Jiang, L., et al. 2014, ApJS, 213, 12

Jiang, L., et al. 2014, ApJS, 213, 12

Jog, C. J., & Combes, F. 2009, Phys. Rep., 471, 75

Johnston, K. V., Bullock, J. S., Sharma, S., Font, A., Robertson, B. E., & Leitner, S. N. 2008, ApJ, 689, 936

Johnston, K. V., Hernquist, L., & Bolte, M. 1996, ApJ, 465, 278

Johnston, K. V., Sackett, P. D., & Bullock, J. S. 2001, ApJ, 557, 137

Kado-Fong, E., et al. 2018, ApJ, 866, 103

Karachentsev, I. D., & Kaisina, E. I. 2022, Astrophysical Bulletin, 77, 372

Karachentsev, I. D., Karachentseva, V. E., Kudrya, Y. N., Sharina, M. E., & Parnovskij, S. L. 1999, Bulletin of the Special Astrophysics Observatory, 47, 5

Katz, N., & Rix, H.-W. 1992, ApJ, 389, L55

Khalid, A., Brough, S., Martin, G., Kimmig, L. C., Lagos, C. D. P., Remus, R. S., & Martinez-Lombilla, C. 2024, MNRAS, 530, 4422

Koda, J., Yagi, M., Yamanoi, H., & Komiyama, Y. 2015, ApJ, 807, L2

Kormendy, J., Fisher, D. B., Cornell, M. E., & Bender, R. 2009, ApJS, 182, 216

Kregel, M., van der Kruit, P. C., & de Grijs, R. 2002, MNRAS, 334, 646

Kron, R. G. 1980, ApJS, 43, 305

Kumar, A., Das, M., & Kataria, S. K. 2021, MNRAS, 506, 98

Lee, Y. W., Joo, J. M., Sohn, Y. J., Rey, S. C., Lee, H. C., & Walker, A. R. 1999, Nature, 402, 55

L'Huillier, B., Combes, F., & Semelin, B. 2012, A&A, 544, A68

Lintott, C., et al. 2011, MNRAS, 410, 166

Łokas, E. L. 2022, A&A, 662, A53

Macciò, A. V., Moore, B., & Stadel, J. 2006, ApJ, 636, L25

Majewski, S. R., Siegel, M. H., Kunkel, W. E., Reid, I. N., Johnston, K. V., Thompson, I. B., Landolt, A. U., & Palma, C. 1999, AJ, 118, 1709

Makarov, D., Prugniel, P., Terekhova, N., Courtois, H., & Vauglin, I. 2014, A&A, 570, A13

Makarov, D., et al. 2022, MNRAS, 511, 3063

Mancillas, B., Duc, P.-A., Combes, F., Bournaud, F., Emsellem, E., Martig, M., & Michel-Dansac, L. 2019a, A&A, 632, A122

—. 2019b, A&A, 632, A122

Marchuk, A. A., Smirnov, A. A., Mosenkov, A. V., Il'in, V. B., Gontcharov, G. A., Savchenko, S. S., & Román, J. 2021, MNRAS, 508, 5825

Marinacci, F., et al. 2018, MNRAS, 480, 5113

Martin, D. C., Matuszewski, M., Morrissey, P., Neill, J. D., Moore, A., Steidel, C. C., & Trainor, R. 2016, ApJ, 824, L5

Martin, G., Kaviraj, S., Devriendt, J. E. G., Dubois, Y., & Pichon, C. 2018, MNRAS, 480, 2266

Martin, G., et al. 2022, MNRAS, 513, 1459

Martínez-Delgado, D., Peñarrubia, J., Gabany, R. J., Trujillo, I., Majewski, S. R., & Pohlen, M. 2008, ApJ, 689, 184

Martínez-Delgado, D., et al. 2010, AJ, 140, 962

—. 2021, MNRAS, 506, 5030

Martinez-Delgado, D., et al. 2021, arXiv e-prints, arXiv:2104.06071

Martínez-Delgado, D., et al. 2023, A&A, 671, A141

Martínez-Lombilla, C., & Knapen, J. H. 2019, A&A, 629, A12

Marziani, P., Dultzin-Hacyan, D., D'Onofrio, M., & Sulentic, J. W. 2003, AJ, 125, 1897

Mateo, M., Olszewski, E. W., & Morrison, H. L. 1998, ApJ, 508, L55

McConnachie, A. W., et al. 2009, Nature, 461, 66

Mihos, J. C., Harding, P., Feldmeier, J., & Morrison, H. 2005, ApJ, 631, L41

Miro-Carretero, J., et al. 2024, arXiv e-prints, arXiv:2409.03585

Miville-Deschênes, M. A., Duc, P. A., Marleau, F., Cuillandre, J. C., Didelon, P., Gwyn, S., & Karabal, E. 2016, A&A, 593, A4

Miville-Deschênes, M.-A., & Lagache, G. 2005, ApJS, 157, 302

Moiseev, A. V., Smirnova, K. I., Smirnova, A. A., & Reshetnikov, V. P. 2011, MNRAS, 418, 244

Morales, G., Martínez-Delgado, D., Grebel, E. K., Cooper, A. P., Javanmardi, B., & Miskolczi, A. 2018, A&A, 614, A143

Mosenkov, A., et al. 2020a, MNRAS, 494, 1751

Mosenkov, A. V., Bahr, S. K. H., Reshetnikov, V. P., Shakespear, Z., & Smirnov, D. V. 2024, A&A, 681, L15

Mosenkov, A. V., Smirnov, A. A., Sil'chenko, O. K., Rich, R. M., Reshetnikov, V. P., & Kormendy, J. 2020b, MNRAS, 497, 2039

Mosenkov, A. V., Sotnikova, N. Y., & Reshetnikov, V. P. 2010, MNRAS, 401, 559

Mosenkov, A. V., et al. 2022, MNRAS, 515, 5698

Naiman, J. P., et al. 2018, MNRAS, 477, 1206

Nelson, D., et al. 2018, MNRAS, 475, 624

—. 2019, Computational Astrophysics and Cosmology, 6, 2

Oh, S. H., Kim, W.-T., & Lee, H. M. 2015, ApJ, 807, 73

Oser, L., Ostriker, J. P., Naab, T., Johansson, P. H., & Burkert, A. 2010, ApJ, 725, 2312

Peñarrubia, J., Navarro, J. F., & McConnachie, A. W. 2008, ApJ, 673, 226

Pedrosa, S. E., Tissera, P. B., & De Rossi, M. E. 2014, A&A, 567, A47

Pillepich, A., Madau, P., & Mayer, L. 2015, ApJ, 799, 184

Pillepich, A., et al. 2018, MNRAS, 475, 648

—. 2019, MNRAS, 490, 3196

Poliakov, D., Mosenkov, A. V., Brosch, N., Koriski, S., & Rich, R. M. 2021, MNRAS, 503, 6059

Pop, A.-R., Pillepich, A., Amorisco, N. C., & Hernquist, L. 2018, MNRAS, 480, 1715

Prieur, J. L. 1990, in Dynamics and Interactions of Galaxies, ed. R. Wielen (Berlin: Springer Berlin, Heidelberg), 72–83

Putman, M. E., et al. 1998, Nature, 394, 752

Qu, Y., Di Matteo, P., Lehnert, M. D., & van Driel, W. 2011, A&A, 530, A10

Quinn, P. J. 1984, ApJ, 279, 596

Reshetnikov, V., Battaner, E., Combes, F., & Jiménez-Vicente, J. 2002, A&A, 382, 513

Reshetnikov, V., & Combes, F. 1998, A&A, 337, 9

—. 2015, MNRAS, 447, 2287

Reshetnikov, V., & Sotnikova, N. 1997, A&A, 325, 933

Reshetnikov, V. P., Mosenkov, A. V., Moiseev, A. V., Kotov, S. S., & Savchenko, S. S. 2016a, MNRAS, 461, 4233

—. 2016b, MNRAS, 461, 4233

Reshetnikov, V. P., Savchenko, S. S., Mosenkov, A. V., Sotnikova, N. Y., & Bizyaev, D. V. 2015, Astronomy Letters, 41, 748

Reshetnikov, V. P., et al. 2025, arXiv e-prints, arXiv:2504.12403

Rich, R. M., Collins, M. L. M., Black, C. M., Longstaff, F. A., Koch, A., Benson, A., & Reitzel, D. B. 2012, Nature, 482, 192

Rich, R. M., et al. 2019, MNRAS, 490, 1539

Rix, H. W., & Katz, N. 1991, in Warped Disks and Inclined Rings around Galaxies, ed. S. Casertano, P. D. Sackett, & F. H. Briggs (Cambridge, UK: Cambridge University Press), 112

Rodruck, M., et al. 2023, MNRAS, 526, 2341

Román, J., Trujillo, I., & Montes, M. 2020, A&A, 644, A42

Sánchez-Saavedra, M. L., Battaner, E., & Florido, E. 1990, MNRAS, 246, 458

Sánchez-Saavedra, M. L., Battaner, E., Guijarro, A., López-Corredoira, M., & Castro-Rodríguez, N. 2003, A&A, 399, 457

Sancisi, R., Fraternali, F., Oosterloo, T., & van der Hulst, T. 2008, A&A Rev., 15, 189

Sanders, J. L., Evans, N. W., & Dehnen, W. 2018, MNRAS, 478, 3879

Schaye, J., et al. 2015, MNRAS, 446, 521

Schlegel, D. J., Finkbeiner, D. P., & Davis, M. 1998, ApJ, 500, 525

Schwarzkopf, U., & Dettmar, R. J. 2000, A&AS, 144, 85

Schweizer, F., Whitmore, B. C., & Rubin, V. C. 1983, AJ, 88, 909

Semczuk, M., Łokas, E. L., D'Onghia, E., Athanassoula, E., Debattista, V. P., & Hernquist, L. 2020, MNRAS, 498, 3535

Seon, K.-I., & Witt, A. N. 2013, ApJ, 778, L40

Simmons, B. D., et al. 2017, MNRAS, 464, 4420

Skrutskie, M. F., et al. 2006, AJ, 131, 1163

Skryabina, M. N., Adams, K. R., & Mosenkov, A. V. 2024, MNRAS, 532, 883

Smirnov, A. A., et al. 2023, MNRAS, 519, 4735

Smith, B. J., Giroux, M. L., Struck, C., & Hancock, M. 2010, AJ, 139, 1212

Smith, B. J., Struck, C., & Pogge, R. W. 1997, ApJ, 483, 754

Sola, E., et al. 2022, A&A, 662, A124

Sollima, A., Gil de Paz, A., Martinez-Delgado, D., Gabany, R. J., Gallego-Laborda, J. J., & Hallas, T. 2010, A&A, 516, A83

Somerville, R. S., & Davé, R. 2015, ARA&A, 53, 51

Springel, V., et al. 2018, MNRAS, 475, 676

Tanaka, M., et al. 2023, PASJ, 75, 986

Thuan, T. X., & Seitzer, P. O. 1979, ApJ, 231, 680

Toomre, A., & Toomre, J. 1972, ApJ, 178, 623

Trujillo, I., & Fliri, J. 2016, ApJ, 823, 123

Valenzuela, L. M., & Remus, R.-S. 2022, arXiv e-prints, arXiv:2208.08443

van der Kruit, P. C. 1979, A&AS, 38, 15

van der Kruit, P. C., & Searle, L. 1981, A&A, 95, 105

van Dokkum, P., et al. 2019, ApJ, 883, L32

van Dokkum, P. G., Abraham, R., Merritt, A., Zhang, J., Geha, M., & Conroy, C. 2015, ApJ, 798, L45

van Eymeren, J., Jütte, E., Jog, C. J., Stein, Y., & Dettmar, R. J. 2011, A&A, 530, A30

Varela-Lavin, S., Gómez, F. A., Tissera, P. B., Besla, G., Garavito-Camargo, N., Marinacci, F., & Laporte, C. F. P. 2023, MNRAS, 523, 5853

Villalobos, Á., & Helmi, A. 2008, MNRAS, 391, 1806

Ward, S. R., Harrison, C. M., Costa, T., & Mainieri, V. 2022, MNRAS, 514, 2936

Weinberg, M. D., & Blitz, L. 2006, ApJ, 641, L33

Whitmore, B. C., Lucas, R. A., McElroy, D. B., Steiman-Cameron, T. Y., Sackett, P. D., & Olling, R. P. 1990, AJ, 100, 1489

Whitney, A., Conselice, C. J., Duncan, K., & Spitler, L. R. 2020, ApJ, 903, 14

Yesuf, H. M., Ho, L. C., & Faber, S. M. 2021, ApJ, 923, 205

Yoon, Y., Ko, J., Chung, H., Byun, W., & Chun, K. 2024, ApJ, 965, 158

Yoon, Y., & Lim, G. 2020, ApJ, 905, 154

York, D. G., et al. 2000, AJ, 120, 1579

Zaritsky, D., Donnerstein, R., Karunakaran, A., Barbosa, C. E., Dey, A., Kadowaki, J., Spekkens, K., & Zhang, H. 2021, ApJS, 257, 60

Zee, W.-B. G., Yoon, S.-J., Moon, J.-S., An, S.-H., Paudel, S., & Yun, K. 2022, ApJ, 935, 48